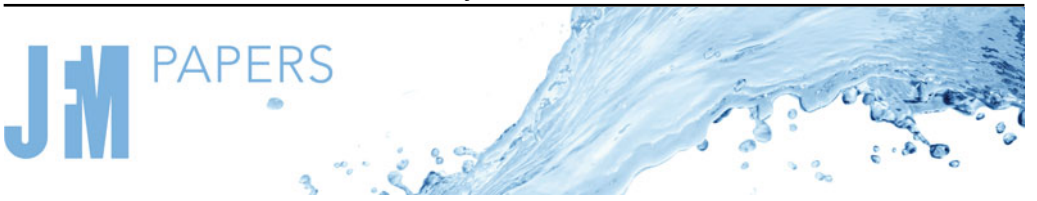
J. Fluid Mech. (2026), *vol.* 1034, A51, doi:10.1017/jfm.2026.11521



Flow interactions and forward flight dynamics of tandem flapping wings

Fang Fang[1], **Christiana Mavroyiakoumou**[1], **Leif Ristroph**[1] and **Michael J. Shelley**[1,2]

[1]Courant Institute of Mathematical Sciences, New York University, 251 Mercer Street, New York, NY 10012, USA

[2]Center for Computational Biology, Flatiron Institute, 162 Fifth Ave, New York, NY 10010, USA

Corresponding author: Christiana Mavroyiakoumou, mavroyiakoum@maths.ox.ac.uk

(Received 15 May 2025; revised 4 April 2026; accepted 5 April 2026)

We examine theoretically the flow interactions and forward flight dynamics of tandem or in-line flapping wings. Two wings are driven vertically with prescribed heaving motions, and the horizontal propulsion speeds and positions are dynamically selected through aero- or hydro-dynamic interactions. Our simulations employ an improved vortex-sheet method to solve for the locomotion of the pair within the collective flow field, and we identify 'schooling states' in which the wings travel together with nearly constant separation. Multiple terminal configurations are achieved by varying the initial conditions, and the emergent separations are approximately integer multiples of the wavelength traced out by each wing. We explain the stability of these states by perturbing the follower and mapping out an effective potential for its position in the leader's wake. Each equilibrium position is stabilised since smaller separations are associated with in-phase follower-wake motions that constructively reinforce the flow but lead to decreased thrust on the follower; larger separations are associated with antagonistic follower-wake motions, increased thrust and a weakened collective wake. The equilibria and their stability are also corroborated by a linearised theory for the motion of the leader, the wake it produces and its effect on the follower. We also consider a weakly flapping follower driven with lower heaving amplitude than the leader. We identify 'keep-up' conditions for which the wings may still 'school' together despite their dissimilar kinematics, with the 'freeloading' follower passively assuming a favourable position within the wake that permits it to travel significantly faster than it would in isolation.

Key words: flow-structure interactions, swimming/flying, vortex dynamics

© The Author(s), 2026. Published by Cambridge University Press. This is an Open Access article, distributed under the terms of the Creative Commons Attribution licence (https://creativecommons.org/licenses/by/4.0/), which permits unrestricted re-use, distribution and reproduction, provided the original article is properly cited.

https://doi.org/10.1017/jfm.2026.11521 Published online by Cambridge University Press

1. Introduction

Flow interactions are thought to play an important role in the locomotion of highly ordered animal groups, such as schools of fish and flight formations of birds. A popular belief is that the group is able to reduce on the energetic cost needed to move through the fluid by taking advantage of the collectively generated flows. For example, individual birds in a V-formation are thought to exploit the upward flow or upwash generated by neighbouring birds to generate the required lift with reduced effort (Lissaman & Shollenberger 1970; Weimerskirch *et al.* 2001; Portugal *et al.* 2014). For fish schools, an increasing number of studies show that individuals in a group gain energetic benefits compared with swimming alone (Belyayev & Zuyev 1969; Zuyev & Belyayev 1970; Svendsen *et al.* 2003; Killen *et al.* 2012). An early theory argues that each fish extracts energy from the vortical flows created by others, and predicts a particularly favourable arrangement is a diamond-shaped lattice (Weihs 1973, 1975). Although this optimal configuration has not been observed in field and laboratory studies (Partridge & Pitcher 1979), efficiency improvement due to vortex–swimmer interactions has been seen in modelling and simulation studies (Hemelrijk *et al.* 2015; Daghooghi & Borazjani 2015).

Studies have made progress by considering the simplified problem of a single body swimming or flying within ambient vortices. Experiments have shown that trout swimming in a von Kármán wake behind a bluff body tend to slalom between vortex cores, and measurements showing reduced muscle activity suggest that flow effects are being exploited (Liao *et al.* 2003; Liao 2007). Theoretical modelling has examined a flexible filament swimming in a vortex street, where the thrust or efficiency can be maximised with respect to the flapping kinematics (Alben 2009*a*, 2010*a*). Other studies focus on a pair of flapping and interacting bodies, for example, a pair of passively flapping filaments (Ristroph & Zhang 2008; Alben 2009*c*, 2012), as well as actively flapping wings or foils placed side-by-side (Dewey *et al.* 2014) or in tandem (Akhtar *et al.* 2007; Boschitsch, Dewey & Smits 2014). Interactions of freely swimming and actively flapping bodies were studied in computational fluid dynamics simulations (Zhu, He & Zhang 2014). A pair of actively flapping and flexible filaments swimming freely in tandem revealed the formation of stable configurations of reduced energetic input. Although Zhu *et al.* (2014) used a somewhat low Reynolds number ($Re = 200$), similar stable configurations of tandem flapping hydrofoils were observed in experiments at the higher Reynolds numbers ($Re = 10^4 \sim 10^5$) typical of schools and flocks (Becker *et al.* 2015; Ramananarivo *et al.* 2016).

By using freely swimming and flapping hydrofoils in controlled experiments, Becker *et al.* (2015), Ramananarivo *et al.* (2016), Newbolt, Zhang & Ristroph (2019) and Newbolt *et al.* (2024) sought to understand the flow interactions relevant to high-Re collective locomotion. These studies build on previous ones that have characterised the locomotion of a single heaving foil (Vandenberghe, Zhang & Childress 2004; Alben & Shelley 2005; Vandenberghe, Childress & Zhang 2006). Such a locomotor leaves a stereotypical thrust wake consisting of an array of staggered and counter-rotating vortices, similar to that seen behind swimming fish (Müller *et al.* 1997). Becker *et al.* (2015) studied the hydrodynamic interactions and swimming dynamics of an in-line array of flapping foils held at fixed separation distances. Constructive and destructive wing–wake interactions were found to coexist and correspond to fast and slow swimming modes of the group, respectively. Introducing the so-called schooling number S, defined as the inter-neighbour separation distance normalised by the wavelength of the swimming trajectory, it was observed that the array assumed S values only between integer to half-integer values, which may be associated with stable wing–wake interactions. This was investigated theoretically by Oza, Ristroph & Shelley (2019) using a discrete-time dynamical system, which showed

https://doi.org/10.1017/jfm.2026.11521 Published online by Cambridge University Press

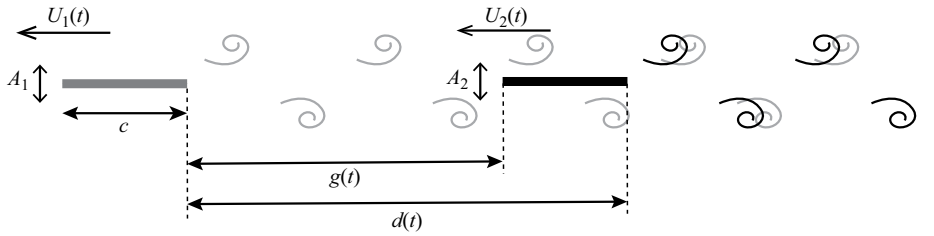


Figure 1. Interaction of a pair of flapping wings in tandem. Two wings, modelled as slender rigid plates, heave with prescribed vertical motions and are individually free to translate in the horizontal direction. Without loss of generality, we assume the wings swim or fly from right to left. Here, A_k is the prescribed heaving amplitude, U_k is the emergent swimming speed (with $k = 1, 2$), c is the chord length of each of the rigid plates, g is the 'tail-head' separation distance and d is the separation distance between the wing centre points (or any equivalent points on the two wings).

good agreement with the experimental data, in particular predicting the bistability of schooling states. The importance of hydrodynamic stability in collective locomotion, heretofore rarely discussed in the literature, was further investigated by Ramananarivo *et al.* (2016) for the case of tandem flapping foils. In this experimental realisation of the simplest 'school of two', the wings are freely swimming and freely spacing. The emergent stable configurations involve the pair travelling together with constant separation and with integer schooling numbers, i.e. the wings maintain a separation distance that is an integer multiple of the motion wavelength. Ramananarivo *et al.* (2016) also measured directly the hydrodynamic restoring forces on the follower and for the first time determined the hydrodynamic potential felt by a locomotor interacting with the wake of a leader. Newbolt *et al.* (2019) investigated the flow interactions between uncoordinated flapping foils with different kinematics, showing that these interactions can spontaneously lead to group cohesion. When the leader and follower flap asynchronously – with a non-zero phase lag ϕ between their heaving motions – the follower settles into one of several discrete positions behind the leader, with the pair subsequently travelling together (Newbolt *et al.* 2019; Mavroyiakoumou, Wu & Ristroph 2025). As ϕ increases, these stable positions are displaced downstream at a constant rate. A recent experimental study involving larger collectives (of up to five foils) demonstrated that chains of increasing size become unstable due to flow-induced instabilities termed flonons (Newbolt *et al.* 2024). In this phenomenon, the horizontal positions of downstream foils begin to oscillate with progressively larger amplitudes down the group, potentially leading to collisions between the trailing members. This instability was subsequently found numerically using a vortex-sheet model in Nitsche, Oza & Siegel (2025).

Inspired by these previous studies, we investigate theoretically the interactions and collective dynamics of a tandem pair of free flapping wings swimming or flying through a fluid. In simulations and a model, we consider two identical and infinitesimally thin plates that are driven up and down vertically (i.e. heaving) in a two-dimensional inviscid and incompressible flow (see figure 1). A follower wing is placed directly downstream of a leader, and the two have identical flapping frequency and temporal phase but perhaps different amplitudes. The wings are individually self-propelled and swim or fly in the horizontal direction, and the two are coupled only through their collective flow field. Our numerical results complement prior work on vortex-sheet simulations of inline flapping plates by Heydari & Kanso (2021) and Nitsche *et al.* (2025), in several ways. Here, we investigate the steady-state velocities and positions of the plates as functions of drag coefficient and heaving amplitude across a wide range of drag coefficients, and we characterise the steady states as potential wells within a potential landscape.

https://doi.org/10.1017/jfm.2026.11521 Published online by Cambridge University Press

In the first half of this paper, we discuss numerical simulations that use a two-dimensional (2-D) vortex-sheet method to study fluid–structure interactions at high Re. We follow the scheme described in Fang *et al.* (2017) that incorporates the fast multipole method (FMM) to efficiently simulate the complex vortical flow fields generated by a dynamic body, and its interaction with these flows. The quadrature rules are improved by applying singularity subtractions and piece-wise analytic evaluations to prevent vortex-sheet penetration at the wing boundaries. The Blasius skin-friction calculation (Schlichting 1968) is coupled with this scheme as a model of viscous drag on each wing, permitting the study of steady states set by force balance. Our simulations confirm previous numerical and experimental results (Zhu *et al.* 2014; Ramananarivo *et al.* 2016; Newbolt *et al.* 2019; Heydari & Kanso 2021) of multiple stable configurations, called 'schooling states' in what follows. We also map out an effective hydrodynamic potential on the follower wing using two strategies, and find the hydrodynamic force on the follower is approximately a sinusoidal function of the schooling number S, defined as the tail-to-head wing separation normalised by the locomotion wavelength. The hydrodynamic potential consists of multiple wells corresponding to the multiple stable states. Investigation of the emergent flow fields shows that, when the follower's flapping motion is in phase with the oscillatory flow left by the leader, the collective wake is constructively reinforced but the follower produces low thrust. In contrast, for out-of-phase motions with the oncoming flow, the follower produces larger thrust as the collective wake is weakened. We show how these effects can be exploited by a follower with low flapping amplitude swimming behind a fast-flapping leader. Surprisingly, this 'freeloading' follower is still able to keep up with the leader, as it passively relocates to a favourable position in the leader's wake. A significant improvement in swimming efficiency is observed in this situation, with the follower even harvesting energy from the wake of the leader.

In the second half of this paper, we calculate analytically the stable states of the two-wing interaction and the hydrodynamic potential on the follower wing using a linearised theory that assumes small flapping amplitude and large wavelength of motion. The linearised Euler equation with a no-penetration boundary condition imposed on a plate was analytically solved by Wu (1961). We combine Wu's solution with a skin-friction model to determine the free-swimming speed of an isolated flapping wing. Motivated by the simulation results, we use the calculations of the isolated wing and its generated wake as approximations to the leader wing and its wake. We then adapt a second calculation of Wu for the thrust on a flapping wing in a wavy stream (Wu 1972; Wu & Chwang 1975) to the interaction of the follower wing with the wavy wake generated by the leader. We provide an analytic expression of the effective hydrodynamic potential on the follower wing, and stable states and the 'keep-up' condition for a low-amplitude follower are also determined. We also include a more comprehensive comparison between the numerical results and these small-amplitude linearised theories. We find excellent agreement in the steady-state velocities and Froude efficiency for a single self-propelled flapping wing, and in the steady-state schooling number for the two-wing case.

2. Simulation method

Efficient simulations of high Reynolds number flows are challenging due to the associated complex vortex dynamics (Saffman 1993). In our study, we use an inviscid 2-D vortex-sheet model to capture both the vorticity distribution along the wings (called the bound sheet, as defined later) and the free vortex wake (the free sheet), as well as the unsteady shedding of vorticity from the wing trailing edge. Within this 2-D model, a vortex sheet is a 1-D boundary across which the fluid normal velocity is continuous while the tangential

https://doi.org/10.1017/jfm.2026.11521 Published online by Cambridge University Press

velocity is not (Rosenhead 1931; Saffman 1993). A stabilised 2-D vortex-sheet model was first proposed by Krasny (1986) using a kernel regularisation technique. Combined with the unsteady Kutta condition, this method is widely used for fluid–structure interaction problems at high *Re*, for example in simulations of a jet flow exiting a tube (Nitsche & Krasny 1994), free falling plates (Jones 2003; Jones & Shelley 2005), passively flapping filaments (Alben & Shelley 2008; Alben 2009*b*) and free flying jellyfish-like machines (Fang *et al.* 2017). In this work, we build on the vortex-sheet formulation for wing-pair interactions and free locomotion described by Fang *et al.* (2017), and we implement a robust numerical algorithm using the FMM. To account for viscous effects and drag, we also include a Blasius skin-friction model (Schlichting 1968). For each individual wing, the balance of the skin-friction drag and computed thrust from the vortex sheet determines the dynamics of the wing in the horizontal direction. We also improve the quadrature rules in the vortex-sheet method, by applying singularity subtractions on the body and piecewise analytic evaluations on the wake, so as to prevent vortex-sheet penetration at the wing boundaries.

2.1. *Modelling*

2.1.1. *Wing model and fluid model*

As shown in figure 1, the pair of wings in tandem are each modelled as rigid plates of the same chord length c. The up-and-down or heaving motions are prescribed by sinusoidal functions of the same frequency f and (perhaps different) amplitudes A_k

$$x_k(s,t) = X_k(t) + s,\ \ s \in [-c/2, c/2], \tag{2.1}$$

$$y_k(t) = A_k \cos(2\pi f t), \tag{2.2}$$

where $k = 1, 2$ denotes the leader and follower wings, respectively, and $\boldsymbol{x}_k = (x_k, y_k)$ denotes their locations. Here, $y_k(t)$ is the same throughout the wing's chord length (i.e. for any $s \in [-c/2, c/2]$ of each wing), and so it is a function of time only. The arc-length parameter s denotes the signed distance from the wing centre $X_k(t) = x_k(0, t)$. The leading edge of the wings (left end of the wing in figure 1) corresponds to $s = -c/2$, and the trailing edge (right end) corresponds to $s = c/2$.

The wings are individually free to swim or fly, that is, to move in the horizontal direction due to hydrodynamic interactions. Assuming a wing mass per unit span of m, the horizontal dynamics of each individual satisfies

$$m\ddot{X}_k = F_k = T_k + D_k, \quad k = 1, 2, \tag{2.3}$$

where F_k is the hydrodynamic force on the wing, composed of the hydrodynamic thrust T_k and drag D_k. Here, the propulsive thrust is negatively signed and the resistive drag is positively signed, given the convention that the wings swim or fly from right to left.

The surrounding inviscid fluid flow is described by the 2-D Euler equations

$$\rho_f \frac{\mathrm{D}\boldsymbol{u}}{\mathrm{D}t} = -\nabla p, \tag{2.4}$$

where $\boldsymbol{u} = (u_x, u_y)$ is the fluid velocity, p is the pressure and ρ_f is the fluid density. We impose a no-penetration boundary condition for the flow velocity $\boldsymbol{u}(\boldsymbol{x}(s))$ on each wing, with the vertical component of the velocity being continuous and matching the wing flapping speed, in a reference frame where the fluid is at rest at infinity. That is, the vertical components $u_{y,\pm}$ above and below the wing are equal to the vertical component of the wing velocity

$$u_{y,+}(\boldsymbol{x}_k(s,t)) = u_{y,-}(\boldsymbol{x}_k(s,t)) = \dot{y}_k(t), \quad k = 1, 2. \tag{2.5}$$

https://doi.org/10.1017/jfm.2026.11521 Published online by Cambridge University Press

In the tangential direction at the wing, i.e. the x-direction, flow is allowed to slip freely along the surface. This horizontal component $u_{x,\pm}(\boldsymbol{x}_k(s,t))$ of the flow velocity can be viewed as a model for the flow just outside of the boundary layer, which approaches zero thickness in the limit of infinite Reynolds number. We later discuss a skin-friction model that estimates the drag due to shear in the viscous boundary layer.

Integration of the fluid pressure over a closed contour around each wing surface C_k^w provides the thrust, i.e. the hydrodynamic force in the horizontal or tangential direction $\hat{\boldsymbol{s}} = (1, 0)$. This integral can be separated into parts associated with an infinitesimal circle (denoted by r_k^{le}) around the wing's leading edge, the differential or jump in pressure $[p]$ across the length of the wing and an infinitesimal circle r_k^{te} at the trailing edge

$$\int_{C_k^w} p\hat{\boldsymbol{n}}\,\mathrm{d}s \cdot \hat{\boldsymbol{s}} = \left(\int_{r_k^{le}} p\hat{\boldsymbol{n}}\,\mathrm{d}s + \int_{-1}^{1} [p]\hat{\boldsymbol{n}}\,\mathrm{d}s + \int_{r_k^{te}} p\hat{\boldsymbol{n}}\,\mathrm{d}s \right) \cdot \hat{\boldsymbol{s}}, \quad \hat{\boldsymbol{s}} = (1, 0). \tag{2.6}$$

In our model, we allow continuous shedding of vorticity at the trailing edge while keeping a flow singularity at the leading edge. The absence of leading-edge shedding is intended as a model applicable to the case of small-amplitude flapping and long wavelengths of motion, in which case the small angles of attack are associated with weak leading-edge separation. The singularity at the leading edge yields a leading-edge suction and thrust in the tangential direction to the wing (Saffman 1993). Note that the integral of the pressure jump $[p]$ along the wing is always normal to the wing and does not contribute to the thrust. The pressure integral around the wing trailing edge is also zero due to the imposition of the unsteady Kutta condition. Therefore, for a heaving wing that swims in a direction parallel to the body axis, the thrust results purely from leading-edge suction. Thus, (2.6) simplifies to

$$T_k = \int_{C_k^w} p\hat{\boldsymbol{n}}\,\mathrm{d}s \cdot \hat{\boldsymbol{s}} = \int_{r_k^{le}} p\hat{\boldsymbol{n}}\,\mathrm{d}s \cdot \hat{\boldsymbol{s}}, \quad \hat{\boldsymbol{s}} = (1, 0). \tag{2.7}$$

The hydrodynamic drag in (2.3) results from skin friction along the upper and lower wing surfaces, which is modelled using Blasius laminar boundary-layer theory (Schlichting 1968, Chap. VII). For one side of a plate in a stream of uniform far-field speed U_f, this approximation gives

$$D_f = 0.664\sqrt{\rho_f \mu c}\,|U_f|^{3/2}, \tag{2.8}$$

where μ is the dynamic viscosity of the fluid. In our model, we replace the free-stream velocity U_f with the tangential flow speed averaged along the wing surface and relative to the swimming speed

$$\overline{U}_{k,\pm}(t) = \frac{1}{c}\int_{-c/2}^{c/2} u_{x,\pm}(\boldsymbol{x}_k(s,t))\,\mathrm{d}s - U_k(t), \tag{2.9}$$

where $U_k(t) = \dot{X}_k(t)$ is the horizontal swimming speed of the wing, which is assumed to move in the negative x-direction (figure 1). Summing the contributions from the upper and lower surfaces of the wing, the total drag is

$$D_k = 0.664\sqrt{\rho_f \mu c}\,\left(|\overline{U}_{k,+}|^{3/2} + |\overline{U}_{k,-}|^{3/2} \right). \tag{2.10}$$

This form of the drag force was also implemented by Heydari & Kanso (2021). We note that the drag force scaling with $U^{3/2}$ reproduces the experimentally observed $(Af)^{4/3}$ dependence of the swimming speed for a single heaving wing (Ramananarivo *et al.* 2016). This is consistent with the scaling identified by Gazzola, Argentina & Mahadevan (2014)

https://doi.org/10.1017/jfm.2026.11521 Published online by Cambridge University Press

for locomotion in the laminar-flow regime at Reynolds numbers up to approximately 10^4 and where drag dominantly arises from skin friction due to laminar boundary-layer flows. At yet higher Reynolds numbers of the turbulent-flow regime, a quadratic drag law of the form U^2 is likely more appropriate and derives from pressure and separated flows (Gazzola *et al.* 2014).

We non-dimensionalise the system with the characteristic length $\tilde{L} = c/2$, time $\tilde{T} = 1/f$, velocity $\tilde{U} = cf/2$ and pressure $P = \rho_f \tilde{U}^2 = \rho_f c^2 f^2/4$. The dimensionless equations of motion are then

$$M\ddot{X}_k = T_k(t) + D_k(t), \tag{2.11}$$

$$y_k(s, t) = \tilde{A}_k \cos(2\pi t), \ \ s \in [-1, 1], \tag{2.12}$$

where

$$T_k = \int_{C_k^w} p\hat{\boldsymbol{n}}\, \mathrm{d}s \cdot \hat{\boldsymbol{s}} \quad \text{and} \quad D_k = C_f \left(\overline{U}_{k,+}^{3/2} + \overline{U}_{k,-}^{3/2}\right), \quad k = 1, 2. \tag{2.13}$$

There are three dimensionless parameters that appear in the system: the wing–fluid mass ratio $M = 4m/(\rho_f c^2)$, the ratio of the heaving amplitude to wing length $\tilde{A}_k = 2A_k/c$ and the skin-friction drag coefficient

$$C_f = 1.878\sqrt{\nu/(c^2 f)}, \tag{2.14}$$

where $\nu = \mu/\rho_f$ is the kinematic viscosity. This drag coefficient is related to the so-called frequency Reynolds number $Re_{fr} = \tilde{L}\tilde{U}/\nu = c^2 f/4\nu$ used in the literature of flapping-wing locomotion (Alben & Shelley 2005): $C_f = 0.939 Re_{fr}^{-1/2}$. When the kinematics, wing chord length and fluid parameters are appropriately matched to the experimental conditions of Ramananarivo *et al.* (2016), (2.14) yields $C_f \sim 0.02$, reproducing the same trends in swimming speed observed in the experiments. In our study, we set the mass ratio to $M = 2$ while exploring the effects of varying $C_f = 0.01$ to 0.1 and $\tilde{A}_k = 0.1$ to 1. Here, the mass per unit span m should be interpreted as the total solid mass of the locomotor (i.e. the free-swimming or flying animal), which sets the relevant inertia for the forward dynamics. We note that, even for an arbitrarily thin wing, a finite value of wing–fluid mass ratio M remains meaningful because it represents the mass payload (e.g. the body of a fish or bird) that is towed by the propulsor (fin or wing). The choice of $M = 2$ is not meant to match a specific biological system; rather, it lies within the range typical of swimming and flying animals (Greenewalt 1962; Rayner 1979; Viscor & Fuster 1987; Dimitriadis *et al.* 2015; Taylor *et al.* 2019; Krishnan *et al.* 2022) and is consistent with flapping-foil experiments and prior numerical studies (Ramananarivo *et al.* 2016; Newbolt *et al.* 2019, 2024; Nitsche *et al.* 2025). A smaller mass, and thus lower inertia, is expected to make the wing more susceptible to fluctuations. This leads to larger oscillations in the separation gap between the wings, which could undermine the positional stabilisation of the wing. The influence of mass will be examined further in future work.

2.1.2. *Vortex-sheet shedding and wake model*

In the vortex-sheet model, a flapping wing is a bound vortex sheet on which the no-penetration boundary condition (2.5) is imposed. The bound sheet encompasses the infinitesimally thin wing and its boundary layers that vanish in thickness at higher Reynolds numbers. At the trailing edge of each wing, a free vortex sheet is continuously shed into the fluid (Nitsche & Krasny 1994). In the free-sheet model the shed shear layer

https://doi.org/10.1017/jfm.2026.11521 Published online by Cambridge University Press

forms downstream eddies. In the limit of zero viscosity, the shed vorticity concentrates onto an infinitesimally thin layer that can be modelled as a 1-D vortex sheet that does not dissipate in time. The vortex shedding rate at the trailing edge is determined by the unsteady Kutta condition (Jones 2003), which provides the direction of vortex shedding as well as the amount of circulation transmitted from the wing (bound sheet) to the wake (free sheet).

In our 2-D vortex-sheet method, we keep track of the sheet position $\zeta_k(s,t)$ as well as the true vortex-sheet strength $\bar{\gamma}_k(s,t)$, defined as the tangential fluid velocity jump across the vortex sheet $\bar{\gamma}_k(s,t) = [\boldsymbol{u}]\hat{s}$ (Shelley 1992). Here, $k = 1, 2$ denotes the two wings, and $s \in [-1, s^k_{max}]$ is an arc-length parameterisation of the vortex sheet. The true vortex-sheet strength $\bar{\gamma}_k(s,t) = \gamma_k(\alpha)/s_\alpha(\alpha,t)$ is related to the (unnormalised) vortex strength $\gamma_k(\alpha)$ which is a material variable, where α is a Lagrangian parameterisation of the sheet. Using complex variables, the vortex-sheet position $\zeta_k(s,t)$ and strength $\bar{\gamma}_k(s,t)$ are related through the Biot–Savart law for the mean velocity of the sheet $w_k(s,t)$

$$\overline{w_k(s,t)} = \frac{1}{2\pi i} \fint_{-1}^{s^k_{max}} \frac{\bar{\gamma}_k(s',t)\,\mathrm{d}s'}{\zeta_k(s,t) - \zeta_k(s',t)} + \sum_{j\neq k} \frac{1}{2\pi i} \int_{-1}^{s^j_{max}} \frac{\bar{\gamma}_j(s',t)\,\mathrm{d}s'}{\zeta_k(s,t) - \zeta_j(s',t)}, \quad (2.15)$$

where the bar denotes the complex conjugate, and $\fint$ is the Cauchy principal value. Since the tangential component of fluid velocity is discontinuous at the vortex sheet, the mean velocity $w_k(s,t)$ is an average of the velocities on the two sides of the sheet boundary $\zeta_k(s,t)$.

The description of the free-sheet boundary $s \in [1, s^k_{max}]$ dynamics is simplified if $w_k(s,t)$ is chosen as a velocity frame, in which case we arrive at the Birkhoff–Rott equation (Shelley 1992)

$$D_t \zeta_k(s,t) = w_k(s,t), \quad 1 \leqslant s \leqslant s^k_{max}, \quad (2.16)$$

where D_t denotes the material derivative, and $w_k(s,t)$ is given by (2.15). Following the Lagrangian path of the free vortex sheet, the circulation $\gamma(\alpha)$ on an infinitesimal segment is conserved

$$D_t(\bar{\gamma}_k(s,t)s_\alpha) = D_t\gamma_k(\alpha) = 0, \quad k = 1, 2. \quad (2.17)$$

The bound vortex-sheet position, i.e. the wing position

$$\zeta_k(s,t) = X_k(t) + s + iy_k(t), \quad s \in [-1, 1], \quad (2.18)$$

is governed by (2.11). Using (2.15), the no-penetration boundary condition of (2.5) yields

$$\mathrm{Im}\,(w_k(s,t)) = \dot{y}_k(t), \quad s \in [-1, 1], \quad (2.19)$$

which is a Fredholm integral equation of the first kind for the bound-sheet strength $\bar{\gamma}_k(s,t)$, $s \in [-1, 1]$.

The unsteady Kutta condition connects the bound and free sheets at the trailing edge (Jones 2003). It requires the vortex shedding to be tangential, i.e. the interface of the bound and free vortex sheets is smooth, and also determines the amount of circulation shed from the bound sheet into the free sheet

$$\dot{\Gamma}_k(t) + [\mathrm{Re}(w_k(1,t)) - U_k(t)]\,\bar{\gamma}_k(1,t) = 0, \quad (2.20)$$

https://doi.org/10.1017/jfm.2026.11521 Published online by Cambridge University Press

where $\Gamma_k(t) = \int_{-1}^{1} \bar{\gamma}_k(s,t)\,\mathrm{d}s$ denotes the total circulation on the bound sheet, and $U_k(t) = \dot{X}_k(t)$ is the wing horizontal swimming speed. Kelvin's circulation conservation theorem ensures that $\Gamma_k(t) = -\int_1^{s^k_{max}} \bar{\gamma}_k(s,t)\,\mathrm{d}s$.

An equation for the pressure jump $[p]_k(s,t)$ distributed on the bound sheet can be derived from the Euler equation (2.4) (Saffman 1993; Jones 2003; Alben 2009*b*) and the Kutta condition (2.20)

$$[p]_k(s,t) = \int_1^s \partial_t \bar{\gamma}_k(s',t)\,\mathrm{d}s' + [\mathrm{Re}(w_k(s,t)) - U_k(t)]\,\bar{\gamma}_k(s,t) + \dot{\Gamma}_k(t). \tag{2.21}$$

Note that the pressure jump across the wing contributes no force in the wing swimming direction, as the wing maintains a horizontal alignment at all times. The thrust arises from the suction force at the wing leading edge (Saffman 1993)

$$T_k(t) = \frac{\pi}{8} v_k^2(-1,t), \tag{2.22}$$

where $v_k(s,t) = \bar{\gamma}_k(s,t)\sqrt{1-s^2}$ has a finite value at $s=-1$ as $\bar{\gamma}_k$ has an inverse square root singularity at the wing leading edge. A full derivation of the leading-edge suction term can be found in Appendix A of Nitsche *et al.* (2025). Note that (2.22) relates the hydrodynamics with the wing dynamics through (2.11).

On each wing, the instantaneous input power $P_{k,in}$ is defined as the product of flapping speed $\dot{y}_k$ and the pressure jump $\int_{-1}^{1}[p]_k\,\mathrm{d}s$, which reflects the energy required to maintain the prescribed flapping motion. The instantaneous output power $P_{k,out}$ equals the rate of work done by the hydrodynamic thrust T_k on the wing at swimming speed U_k. Hence,

$$P_{k,in}(t) = -\dot{y}_k(t) \int_{-1}^{1} [p]_k(s,t)\,\mathrm{d}s, \tag{2.23}$$

$$P_{k,out}(t) = T_k(t)U_k(t) = \frac{\pi}{8} v_k^2(-1,t)U_k(t). \tag{2.24}$$

The ratio of $P_{k,in}$ and $P_{k,out}$ gives the Froude efficiency on each wing $\eta_k,\ k=1,2$ and also the efficiency for the pair η (Lighthill 1960; Wu 1961)

$$\eta_k = \frac{\langle P_{k,out}\rangle}{\langle P_{k,in}\rangle}, \quad \eta = \frac{\langle P_{1,out}\rangle + \langle P_{2,out}\rangle}{\langle P_{1,in}\rangle + \langle P_{2,in}\rangle}, \tag{2.25}$$

where $\langle\cdot\rangle = \int_t^{t+1}(\cdot)\,\mathrm{d}t'$ denotes the time average over a flapping stroke.

In the end, we express the mean tangential flow speed along the wing $\overline{U}_{k,\pm}(t)$ (2.9) using vortex-sheet variables in order to calculate the skin-friction drag D_k of (2.13). By the definitions of the mean velocity $w_k(s,t)$ and vortex-sheet strength $\bar{\gamma}_k(s,t)$, the tangential speed along the two surfaces of each wing $u_{x,\pm}(\zeta_k(s,t))$ satisfies

$$\begin{aligned} u_{x,+}(\zeta_k(s,t)) + u_{x,-}(\zeta_k(s,t)) &= 2\mathrm{Re}(w_k(s,t)), \\ u_{x,+}(\zeta_k(s,t)) - u_{x,-}(\zeta_k(s,t)) &= \bar{\gamma}_k(s,t), \end{aligned} \tag{2.26}$$

from which we obtain

$$u_{x,\pm}(\zeta_k(s,t)) = \mathrm{Re}(w_k(s,t)) \pm \frac{1}{2}\bar{\gamma}_k(s,t). \tag{2.27}$$

Substituting (2.27) into (2.9), $\overline{U}_{k,\pm}(t)$ is then expressed as

$$\overline{U}_{k,\pm}(t) = \frac{1}{2}\int_{-1}^{1} \mathrm{Re}(w_k(s,t))\,\mathrm{d}s - U_k(t) \pm \frac{1}{4}\int_{-1}^{1} \bar{\gamma}_k(s,t)\,\mathrm{d}s. \tag{2.28}$$

https://doi.org/10.1017/jfm.2026.11521 Published online by Cambridge University Press

2.2. *Numerical schemes*

Our numerical schemes follow closely those described by Fang *et al.* (2017) and build on similar methods that have been used to study single slender bodies undergoing unsteady motions at high Reynolds numbers (Jones & Shelley 2005; Alben & Shelley 2008; Alben 2009*b*). For the two-body interaction problem studied here, the follower's body interacts with the vortex sheet shed by the leader. To prevent the sheet from penetrating the wing due to numerical errors, an accurate quadrature rule is required. In our simulations, we improve the numerical vortex-sheet method developed by Alben (2009*b*, 2010*b*) and Fang *et al.* (2017) by applying a singularity subtraction method for the singular integral kernel on the bound vortex sheet and a piece-wise quadrature on the free sheets (see Appendix A). Moreover, the vortex-sheet scheme is combined with the skin-friction computation in our simulations to permit the study of steady-state motions that arise from force balance. In what follows, we outline the main steps of the numerical schemes.

We assume the fluid is initially at rest. The wings are initialised with horizontal velocity $U_1(0) = U_2(0) = U_0$ and wing–wing separation $x_2(0) - x_1(0) = d_0$, where $d_0 = d(0)$, and $d(t)$ is defined as the horizontal separation between equivalent points on the two wings (see figure 1). The vortex-sheet strength is initially zero, and the free sheets are confined to the wing trailing edges, i.e. $\bar{\gamma}_k(s,t)|_{t=0} = 0, \quad s \in [-1, 1]$ and $s^k_{max}|_{t=0} = 1$. After initialisation, at each time step we update the vortex sheets in two steps: (a) update the existing free sheets $(\zeta_{f,k}, \bar{\gamma}_{f,k})$ by an explicit scheme; (b) solve and update the bound sheets $(X_k, \bar{\gamma}_{b,k})$ and wing circulation Γ_k through an implicit nonlinear Broyden solver (Broyden 1965), and shed a vortex-sheet segment at the trailing edge into the free vortex sheet. Here, the subscripts f and b denote the free and bound sheets, respectively.

The free vortex sheets are discretised by Lagrangian points $\zeta^{j,n}_{f,k}, \ 0 \leqslant j \leqslant n$ at time t_n. At each time step t_j, a new vortex-sheet segment $[\zeta^{j-1,j}_{f,k}, \zeta^{j,j}_{f,k}]$ is produced at each wing trailing edge (no segment shed at t_0). The dynamics of the free sheet follows (2.16) and is numerically updated by a second-order explicit Adams–Bashforth method, except for the last segment which is newly generated at the last time step and is updated using an explicit Euler scheme. Based on (2.17), the vortex circulation on each vortex-sheet segment is conserved. Following this, on segment $[\zeta^{j-1,n}_{f,k}, \zeta^{j,n}_{f,k}]$ the true vortex-sheet strength (circulation density) $\bar{\gamma}^{j,n}_{f,k}, 1 \leqslant j \leqslant n$, is calculated by dividing the circulation of the segment by the segment length. For the newly generated segment at time t_{n+1}, $[\zeta^{n,n+1}_{f,k}, \zeta^{n+1,n+1}_{f,k}]$, the last end point $\zeta^{n+1,n+1}_{f,k}$ is the same as the wing trailing edge at time t_{n+1}, and the circulation of the last segment is equal to $-(\Gamma^{n+1}_k - \Gamma^n_k)$, where both the trailing edge $\zeta^{n+1,n+1}_{f,k}$ and wing circulation Γ^{n+1}_k at time t_{n+1} are solved in the implicit step next.

The bound vortex sheet, i.e. the flapping wing, is discretised using $m+1$ Chebyshev–Gauss–Lobatto nodes

$$s_j = \cos(\phi_j), \ \phi_j = \frac{j\pi}{m}, \quad j = 0, \ldots, m, \tag{2.29}$$

and the smooth function $\nu_k(s,t) = \bar{\gamma}_k(s,t)\sqrt{1-s^2}$ is approximated by the mth-order polynomial interpolated at s_i. Once the free sheets are updated, in the implicit step the wing position and speed $(X^n_k, U^n_k) \approx (X_k(t_n), U_k(t_n))$, bound-sheet strength $\nu^{i,n}_k \approx \nu_k(s_i, t_n)$ and wing circulation $\Gamma^n_k \approx \Gamma_k(t_n)$ are solved to match the updated free vortex sheets. The Cauchy singular integral (2.19) and Kutta condition (2.20) together provide $2(m+1)$ equations for the variables $\nu^{i,n}_k, \ i = 1, \ldots, m$ and $\Gamma^n_k \approx \Gamma_k(t_n)$ (see Golberg

https://doi.org/10.1017/jfm.2026.11521 Published online by Cambridge University Press

2013; Alben 2009*b*; Fang *et al.* 2017). The wing dynamical variables (see (2.11)) are discretised by a second-order Crank–Nicolson scheme, which then provides 4 equations for (X_k^n, U_k^n)

$$0 = X_k^{n+1} - X_k^n - \frac{\triangle t}{2}(U_k^{n+1} + U_k^n), \quad 0 = U_k^{n+1} - U_k^n - \frac{\triangle t}{2M}(F_k^{n+1} + F_k^n), \quad k = 1, 2, \tag{2.30}$$

where $F_k^n \approx F_k(t_n) = T_k(t_n) + D_k(t_n)$ is the horizontal component of force on the wing, calculated using (2.13), (2.22) and (2.28). This completes a nonlinear system for $2(m+1)+4$ variables for the bound vortex sheets. Using Broyden's method, the solution is found to converge to 10^{-10} in about 10∼15 iterations.

Some additional implementation details are worth noting. First, in the Birkhoff–Rott equation, (2.16), a regularised kernel (Krasny 1986)

$$\mathcal{K}_\delta(s, s') = \frac{\overline{\zeta_k(s,t) - \zeta_k(s',t)}}{|\zeta_k(s,t) - \zeta_k(s',t)|^2 + \delta^2(s)} \tag{2.31}$$

is applied on the free vortex sheets, which suppresses instabilities and resolves the ill-posedness of the free-sheet dynamics (Moore 1979; Shelley 1992). The regularisation is singular on the bound vortex sheet. To resolve discontinuities at the wing trailing edge, the smoothing function $\delta(s)$ is defined using the velocity smoothing treatment developed by Alben (2010*b*). Its form is given by

$$\delta(s) = \begin{cases} \delta_1 + (\delta_0 - \delta_1)\dfrac{|(s-1)/\eta_1|^p}{1 + |(s-1)/\eta_1|^p}, & s \in (1, s^k_{max}], \\ \delta_1 e^{-|(s-1)/\eta_2|^p}, & s \in [-1, 1], \end{cases} \tag{2.32}$$

where $\delta_0 = 0.2$, $\delta_1 = 0.1$, $\eta_1 = 2\delta_0$, $\eta_2 = 0.1$ and $p = 2$. The smoothing function $\delta(s)$ approaches δ_0 for $|s-1| \gg \eta_1$. As each time step introduces a new vortex segment into the free sheet from each wing, the number of points on the free sheets increases linearly in time. For computational efficiency, we approximate the far-field vortex sheets using point vortices, the error introduced being of order $O(1/r)$, where r is the distance to the wing. Using $\triangle t = 0.01$, the number of points needed to resolve the near-field free vortex sheets is approximately $10^3 \sim 10^4$. In practice, we employ the point-vortex approximation for the free vortex sheets at regular time intervals (e.g. every 50 time steps). The free vortex sheet is first partitioned into consecutive segments of uniform circulation sign by examining the differences in circulation strength between adjacent mesh points. These segments, defined by their start and end indices along the sheet, correspond to regions of positive or negative circulation. Each segment exceeding a prescribed arc-length threshold is then replaced by a single point vortex that is located at the circulation-weighted centre of vorticity of that segment, with circulation equal to the total circulation of the replaced portion. This ensures the conservation of vorticity. In our numerical scheme, we also add point vortices in regions where vortex spacing exceeds a critical value, using interpolation. Conversely, point vortices that approach closer than a specified fraction of a characteristic length scale are selectively removed to avoid excessive clustering. This adaptive insertion and deletion, combined with periodic conversion of far-field sheet segments into point vortices, provides an efficient method of computing the vortex-sheet evolution. To speed up the integral evaluations, we use an adaptive kernel-independent FMM for the regularised kernel (2.31) (Fang *et al.* 2017), and a 2-D FMM for the original Laplace kernel $\mathcal{K}(s, s') = 1/(\zeta_k(s,t) - \zeta_k(s',t))$ (Carrier, Greengard & Rokhlin 1988). In the latter, we note that the interaction is very singular when the follower gets close to

https://doi.org/10.1017/jfm.2026.11521 Published online by Cambridge University Press

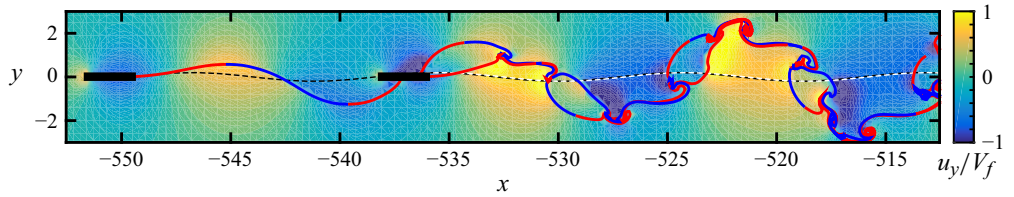


Figure 2. A movie snapshot from one typical simulation. In this example, the two wings have the same flapping amplitude $\tilde{A} = 0.2$ and the drag coefficient is fixed at $C_f = 0.02$. Vortex sheets are shed continuously from the wing trailing edges (red for positive vortex-sheet strength and blue for negative). The colour map represents the vertical component u_y of flow velocity normalised by the flapping speed $V_f = 2\pi Af$. Trajectories of the leader's trailing edge (black dashed line) and follower's leading edge (white dashed line) are marked and seen to overlap. We note that the follower wing can slice into the leader's vortex wake, but this is a discretisation and visualisation artefact, and not a violation of the no-penetration boundary condition (2.5). See supplementary movie.

the free vortex sheet shed from the leader, thus accurate quadrature rules are necessary here to prevent the free sheet from penetrating the bound sheet. In our simulations, we apply a singularity subtraction method for the singular integral kernel $\mathcal{K}(s, s')$ to evaluate the induced velocities by a bound sheet on the other wing's bound or free sheet, and a piece-wise quadrature to compute the velocity induced by a free vortex sheet on another wing's bound or free sheet. Details are provided in Appendix A. At the final time of the simulations, the total number of points processed by the FMM is of the order of several thousand, although the precise count depends on the physical parameters and initial conditions. In all cases, each wing's bound vortex sheet is discretised using 81 points, the far field is represented by $O(10^2)$ merged point vortices per wing, and the near-field free sheets retain $O(10^3)$ points per wing after adaptive merging and deletion. Therefore, the total number of points involved in the FMM at final time is $O(10^3 - 10^4)$.

3. Simulation results

3.1. *Steady-state locomotion*

We begin by seeking the steady-state motions of two tandem wings with identical flapping amplitudes $\tilde{A}_1 = \tilde{A}_2 = \tilde{A}$. We initialise the swimming speeds U_k by the stroke-averaged speed $\langle U_0 \rangle$ of an isolated single wing with the same $\tilde{A}$ and drag coefficient C_f, i.e. $U_1(0) = U_2(0) = \langle U_0 \rangle$. Fixing $\tilde{A} = 0.2$ and $C_f = 0.02$, we vary the initial separation between the wings $d_0 = d(0) = x_2(0) - x_1(0)$, where d denotes the separation distance between the wing centre points (or any equivalent points on the two wings, as in figure 1). As the simulation starts, the two wings interact with each other through the surrounding fluid, and the horizontal motion of each body is determined by the resulting hydrodynamic forces. The pair may eventually arrive at what seems to be a steady-state condition, and an example snapshot of the emergent configuration and flow field is shown in figure 2. The pair swims or flies together at the same average speed and the two wings maintain a nearly constant separation distance.

We examine 11 values of $d_0 \in [4, 44]$ and find several such 'schooling' modes of fixed and finite steady-state separation distance d, as shown in figure 3(*a*). Pairs initialised with $d_0 = 12, 16, 28, 32, 40, 44$ lock onto these states, while $d_0 = 4, 8, 20, 24, 36$ leads to 'rear-ending' collisions between the wings (and termination of the simulation). In figure 3(*a*), initial separation distances d_0 that result in steady-state separation distances are shown in colour (with distinct colours for each d_0), and those that lead to collisions

https://doi.org/10.1017/jfm.2026.11521 Published online by Cambridge University Press

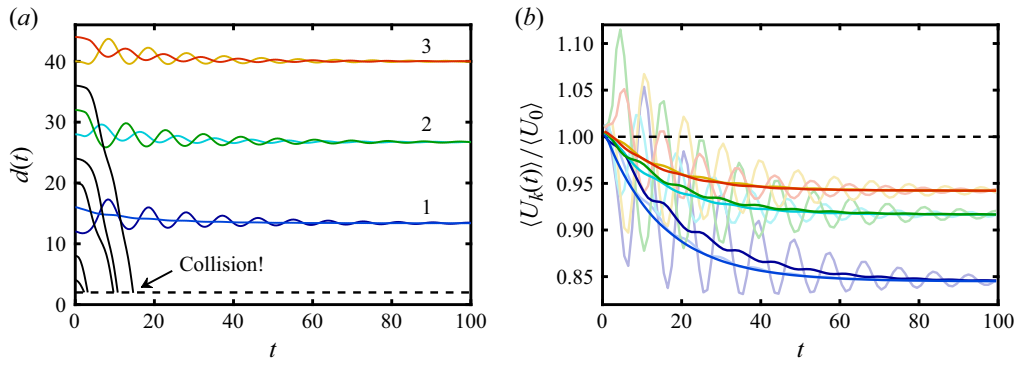


Figure 3. Steady-state locomotion of the pair for different initial wing separations. The two wings have the same flapping amplitude $\tilde{A} = 0.2$ and the drag coefficient is fixed at $C_f = 0.02$. The swimming speeds of both wings are initialised by the stroke-averaged speed of an isolated single wing $\langle U_0 \rangle$. Among these simulations, pairs with initial separation distances of $d_0 = 12, 16, 28, 32, 40, 44$ are locked into 'schooling states' in which the group travels together with nearly constant separation d. Rear-ending collisions occur for $d_0 = 4, 8, 20, 24, 36$. (*a*) Instantaneous wing separation $d(t) = x_2(t) - x_1(t)$. The initial separation distances d_0 that lead to collisions are labelled by the black curves. The first three steady schooling states 1, 2, 3 are displayed. (*b*) Stroke-averaged velocity of the leader wing $\langle U_1 \rangle$ (dark colours) and follower wing $\langle U_2 \rangle$ (light colours), normalised by the single-wing velocity $\langle U_0 \rangle$.

are represented by black curves. The stroke-averaged swimming velocity $\langle U_k \rangle$, $k = 1, 2$ is shown in figure 3(*b*), which is normalised by the single-wing speed $\langle U_0 \rangle$. After the initialisation, the leader wing slows down nearly monotonically in its approach to the terminal or steady-state velocity, while the follower's velocity $\langle U_2 \rangle$ shows oscillations in its approach to this same speed. Previous studies observed collisions between two wings only under limited conditions (Heydari & Kanso 2021; Nitsche *et al.* 2025). Differences in the drag model formulation, choice of parameters and the systematic exploration of initial separations may explain why collisions were not reported more generally. In particular, both studies considered parameter values (M, $\tilde{A}$ and C_f) that differ from ours, Nitsche *et al.* (2025) used a different drag model, while Heydari & Kanso (2021) employed a similar model but did not vary initial conditions systematically, potentially missing the collision regimes we identify in the current work.

The locomotion modes of interacting flapping wings can be quantified by the so-called schooling number (Becker *et al.* 2015; Ramananarivo *et al.* 2016; Newbolt *et al.* 2019), defined as $S = \langle g \rangle / \lambda$, which represents the stroke-averaged inter-swimmer separation $\langle g \rangle = \langle d \rangle - c$ (see figure 1) normalised by the wavelength $\lambda = \langle U_1 \rangle / f$ of the leader's path through the fluid. Here, the normalised chord length is $c = 2$ and normalised flapping frequency is $f = 1$. The schooling number S is a dimensionless quantity that represents the relative phase of the follower's motion to the leader's. As figure 4 shows, the schooling number S approaches steady-state or terminal values $S = S_1, S_2, S_3$ that are close to integer values. This indicates that the motion of the follower's leading edge is nearly in phase spatially with that of the leader's trailing edge. This steady-state condition is made apparent in figure 2, where the trajectories of the leader's trailing edge (black dashed curve) and the follower's leading edge (white) are seen to overlap. We note that more schooling states with higher values of S exist and can be arrived at by considering greater initial separation distances d_0. This has been observed in a recent numerical study that also employs a vortex-sheet method (Nitsche *et al.* 2025).

For all the steady schooling states, we find that the terminal swimming speed is somewhat less than the single-wing speed $\langle U_0 \rangle$, as shown in figure 5(*a*). The decrease

https://doi.org/10.1017/jfm.2026.11521 Published online by Cambridge University Press

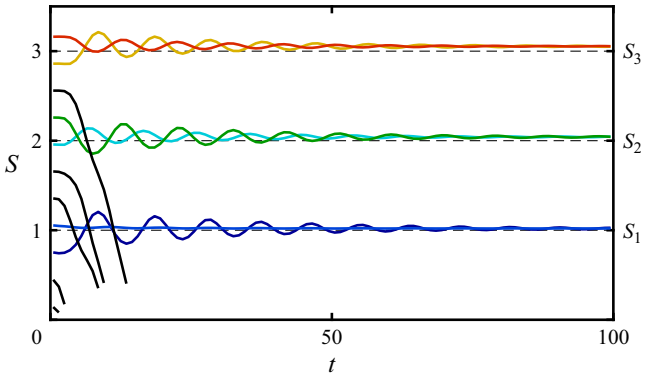


Figure 4. Characterising the steady-state modes using the so-called schooling number. The instantaneous schooling number is defined as $S = \langle g \rangle / \lambda$, where $\langle g \rangle = \langle d \rangle - c$ is the inter-wing gap distance and $\lambda = \langle U_1 \rangle / f$ is the wavelength of the leader's path through the fluid. The steady-state or terminal values S_1, S_2, S_3 are close to the integers, i.e. there are an integer number of swimming wavelengths separating the two wings. The cases for which the initial separation distances lead to a collision are highlighted in black, similar to figure 3(*a*).

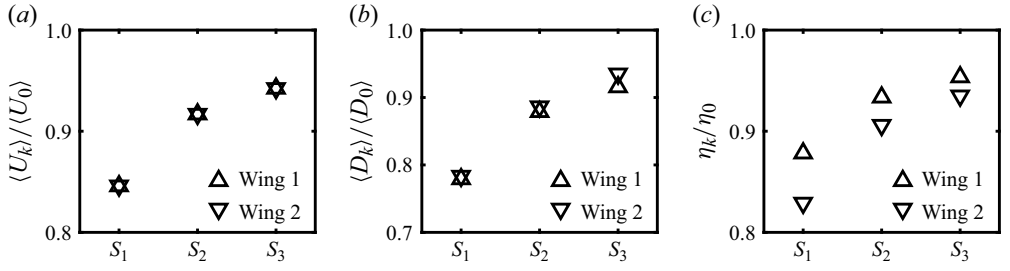


Figure 5. Comparing speed, drag and efficiency for schooling states $S = S_1, S_2, S_3$ to swimming in isolation. (*a*) Stroke-averaged terminal swimming speed normalised by single-wing speed $\langle U_k \rangle / \langle U_0 \rangle$. (*b*) Stroke-averaged drag at steady state normalised by single-wing drag $\langle D_k \rangle / \langle D_0 \rangle$. (*c*) Froude efficiency normalised by single-wing efficiency η_k / η_0.

in swimming speed leads to a lower skin-friction drag $\langle D_k \rangle \lesssim \langle D_0 \rangle$ (figure 5*b*), and also a lower efficiency $\eta_k \lesssim \eta_0$ (figure 5*c*). The speed, drag and efficiency are smaller for the lower S states when the wings are closer and interactions presumably stronger, and these quantities approach the single-wing values for greater S. In this respect, the interactions may be viewed as detrimental, as the two individuals would move faster and with greater efficiency if they were in isolation or were widely separated.

3.2. *Varying relevant parameters*

Next, we vary some relevant model parameters and examine their effect on the first three schooling states. The flapping amplitude remains identical between the two wings and is varied over $\tilde{A} = 2A/c = 0.1$ to 1, and the drag coefficient over $C_f = 0.01$ to 0.1. We note that varying $\tilde{A}$ and C_f is equivalent to changing the wing kinematics, i.e. changing flapping amplitude A and frequency f, since $C_f = 1.878\sqrt{\nu/(c^2 f)}$ per (2.14). For each parameter pair $(\tilde{A}, C_f)$, we initialise the wing speeds using the steady-state speed of the single wing with the same $(\tilde{A}, C_f)$, i.e. $U_1(0) = U_2(0) = \langle U_0 \rangle$, and the separation distance is initialised such that the initial schooling numbers are integer values.

https://doi.org/10.1017/jfm.2026.11521 Published online by Cambridge University Press

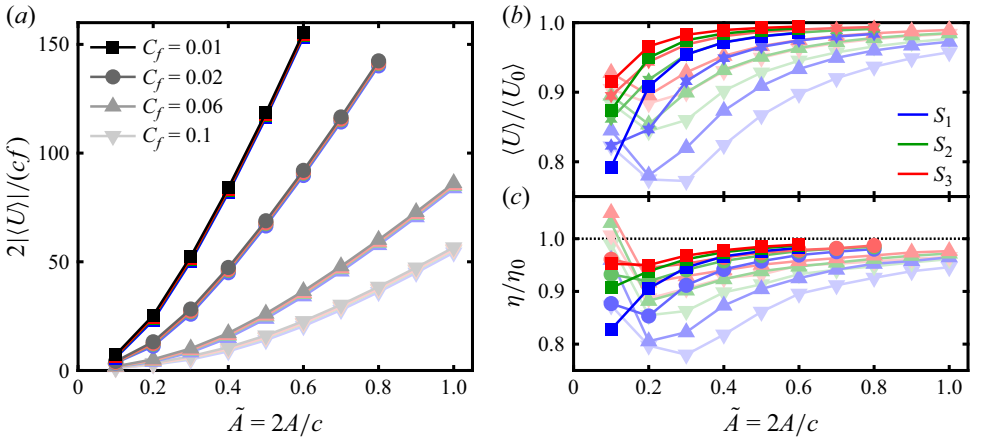


Figure 6. Comparisons between the steady-state swimming of a pair (coloured curves) and a single wing (black and grey curves), for various flapping amplitudes $\tilde{A}$ and friction coefficients C_f. (*a*) Dimensionless steady-state and stroke-averaged swimming speed $2|\langle U\rangle|/(cf)$. (*b*) Terminal swimming speed of the pair normalised by single-wing speed $\langle U\rangle/\langle U_0\rangle$. (*c*) Froude efficiency of the pair normalised by the single-wing efficiency η/η_0.

For each parameter pair $(\tilde{A}, C_f)$, we arrive at three steady states corresponding to the three initial values of $S_0 = 1, 2, 3$. The steady states can be characterised by the stroke-averaged terminal speed and schooling number $(\langle U\rangle, S_k)$ with $k = 1, 2, 3$, as displayed in figures 6 and 7. As shown by the black curves in figure 6(*a*), the steady speed of single wing $\langle U_0\rangle$ is a function of the wing flapping amplitude and drag coefficient $(\tilde{A}, C_f)$, which is determined by the thrust and drag balance on the wing. For the same $(\tilde{A}, C_f)$, the steady speed of the school $\langle U\rangle$ does not vary much from the single-wing speed $\langle U_0\rangle$. Moreover, figure 6(*b*) shows that the pair speed is always slightly slower than that of an individual, with a decrease of up to 23 % for the parameter range we examine. The Froude efficiency of the group η (computed using (2.25)), shown in figure 6(*c*), is also found to be somewhat lower than the single-wing efficiency η_0 for most cases. For some conditions, such as $(\tilde{A}, C_f) = (0.1, 0.06)$ and $(\tilde{A}, C_f) = (0.1, 0.1)$, the efficiency is slightly higher (up to 5 %) than the single-wing efficiency, an example of the group exploiting flow interactions to improve propulsive efficiency.

We next consider how the steady-state schooling numbers vary with changing kinematic parameters. In figure 7 we display S as a function of normalised wavelength $\lambda/c = \langle U\rangle/(cf)$, which varies due to changes in the flapping amplitude $\tilde{A}$ and drag coefficient C_f. For all but the smallest wavelengths, the schooling numbers S_k tend to take on approximately integer values at moderate λ/c and monotonically increase toward integer-and-a-quarter values for large λ/c. These results show that, for sufficiently large wavelength, the motions of the follower's leading edge and the leader's trailing edge are nearly in phase spatially, with a phase lag smaller than a quarter. This result is made more apparent in figure 7(*b*), where we consider the schooling number modulo the associated integer value $S_k - k$. Comparing these results with experiments (Ramananarivo *et al.* 2016), we see a strong correspondence in that the values of S_k are close to integers for the experimentally accessed range of $\lambda/c = 1$ to 8 (see the inset of figure 7*b*). These results are also in excellent agreement with recent simulations by Nitsche *et al.* (2025), which, for a narrower range of kinematic parameters and a fixed skin-friction coefficient, found that the first schooling state is slightly greater than 1, with subsequent schooling states increasing approximately by integer increments; that is $S_k \approx S_{k-1} + 1$.

https://doi.org/10.1017/jfm.2026.11521 Published online by Cambridge University Press

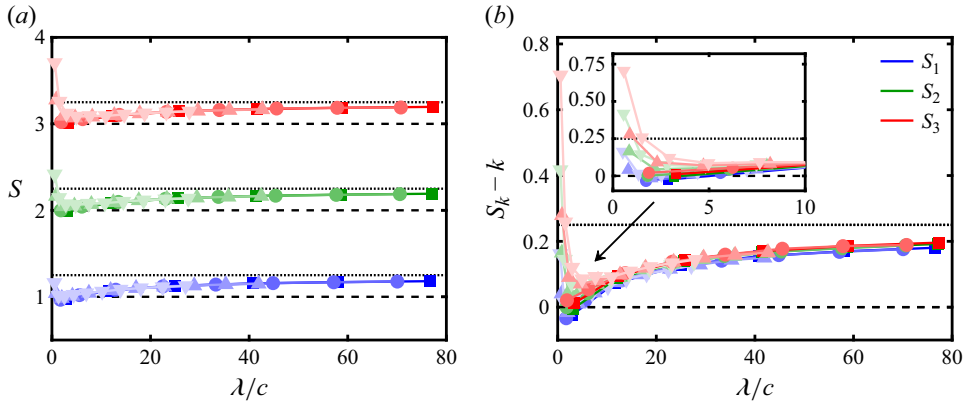


Figure 7. Steady-state schooling numbers as functions of the normalised swimming wavelength λ/c. The flapping-wing amplitude $\tilde{A}$ and drag coefficient C_f are varied to arrive at different λ. (*a*) Three steady-state schooling numbers S_1, S_2, S_3 are achieved for each parameter pair $(\tilde{A}, C_f)$. Except for small $\lambda/c \lesssim 2$, S_k lies between integer and integer-and-a-quarter values. (*b*) Schooling numbers modulo the integers for states labelled $k = 1, 2, 3$, versus the normalised swimming wavelength λ/c.

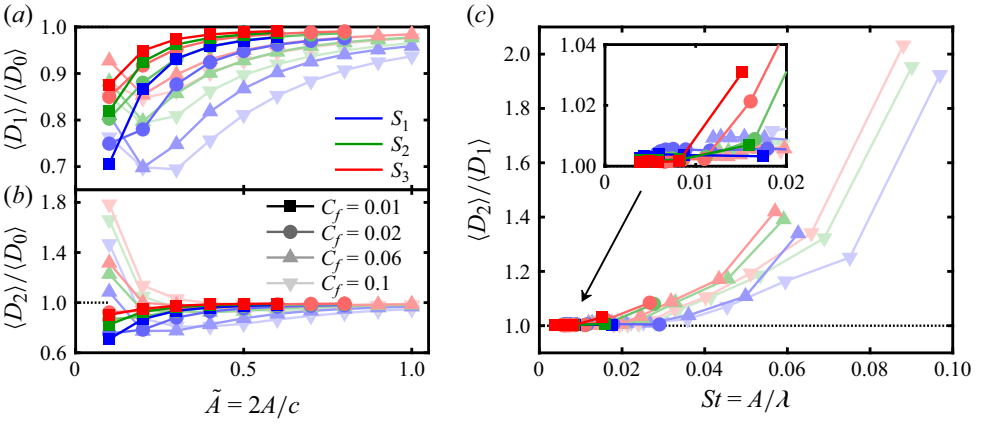


Figure 8. (*a*) Drag force $\langle D_k\rangle$ experienced by (*a*) the leader ($k = 1$) and (*b*) the follower ($k = 2$), normalised by the single-wing drag $\langle D_0\rangle$, for various flapping amplitudes $\tilde{A}$ and friction coefficients C_f. (*c*) Follower-to-leader drag ratio, $\langle D_2\rangle$, against the Strouhal number, $St = A/\lambda$.

The drag on each of the wings is characterised in figure 8. The leader's drag is always less than that of a single wing for the same parameters, as shown by the plot of $\langle D_1\rangle/\langle D_0\rangle$ in figure 8(*a*). While it may be surprising that the leader's forces are at all affected by the presence of the follower, the drag reduction is consistent with the reduction in swimming speed $\langle U_1\rangle \lesssim \langle U_0\rangle$ for the pair relative to an isolated individual (figure 6). This result also implies, by force balance, a reduced thrust for the leader. The follower, on the other hand, may experience less or more drag compared with a single wing, depending on the values of the parameters $\tilde{A}$ and C_f, as shown in figure 8(*b*). Cases of lower drag may again be explained by noting the reduced swimming speed of the pair relative to an individual. Cases of higher drag arise only for high C_f, where we expect the higher skin friction to be balanced by higher thrust and consequently stronger wake flows. This suggests that the high drag on the follower may be related to the strong jet-like flow produced by the leader.

https://doi.org/10.1017/jfm.2026.11521 Published online by Cambridge University Press

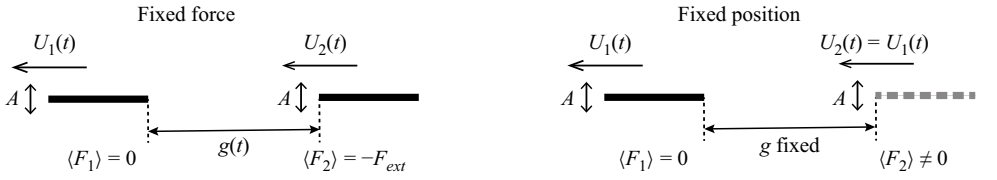


Figure 9. Two methods to map out the interaction of the follower with the leader's wake. (*a*) Applying an external force F_{ext} on the follower. At the new equilibrium, the total hydrodynamic force is zero on the leader while the hydrodynamic force on the follower is equal and opposite to the external load. (*b*) 'Ghost follower method.' Fixing the position where the follower sits relative to the leader. A fixed separation $g(t) = g_0$ is maintained by prescribing the follower dynamics to match the leader's, $U_2(t) = U_1(t)$. At the new equilibrium, the hydrodynamic thrust and drag balance on the leader but not on the follower.

We investigate this idea in figure 8(*c*), where the follower-to-leader drag ratio is plotted against the Strouhal number, defined as $St = Af/\langle U\rangle = A/\lambda$. Low St is associated with weak jet-like flows in the wake of a self-propelled flapping body – the extreme of $St = 0$ being a purely translating body that injects no momentum into the wake – while high St is associated with strong wake flows. Indeed, from figure 8(*c*) we see that the follower's drag can be as high as twice that of the leader, and that this occurs only at high St where we expect a strong wake generated by the leader.

We note that for the Strouhal numbers observed here, the maximum effective angle of attack $\alpha_{max} = \tan^{-1}(2\pi Af/U_\infty) = \tan^{-1}(2\pi St)$, is generally well below 10°, while the instantaneous angle of attack (Shyy *et al.* 2010), $\alpha(t) = \tan^{-1}(-\dot{y}(t)/U_\infty)$, with $\dot{y}(t) = -2\pi Af\,\sin(2\pi ft)$, is necessarily smaller. Consequently, this supports the validity of our model, which allows shedding of vorticity only at the trailing edge of the wing. The wing only reaches this 'worst-case' angle briefly around midstroke, leaving insufficient time for significant vorticity to develop and be shed.

3.3. *Hydrodynamic potential*

The above results show that, as the pair approaches a steady state, the follower wing relaxes to its equilibrium position with damped oscillations (figure 3*b*). This indicates that the hydrodynamic force on the follower acts as a restoring force that stabilises each observed position within the leader's wake, suggesting a description in terms of a stability potential. In this view, the multiple stable positions seen in our simulations suggest a corrugated potential landscape with an array of stable wells.

To test these ideas, we map out the hydrodynamic force and potential for the follower by two methods. First, we apply a constant external load or force F_{ext} on the follower wing (figure 9*a*). As will be shown, for sufficiently small F_{ext}, the wings adjust their swimming dynamics and relax to new equilibrium values for the speed, gap distance and schooling number. At the new equilibrium state, the time-averaged thrust and drag forces are balanced on each wing, and thus the total force on each is zero: for the leader $\langle F_1\rangle = 0$ and for follower $\langle F_2\rangle = -F_{ext}$. At each new equilibrium obtained by varying F_{ext}, we extract the new steady speed of the school $\langle U\rangle$, the schooling number S, the total force on the follower $\langle F_2\rangle$, as well as its thrust $\langle T_2\rangle$ and drag $\langle D_2\rangle$. In figure 10(*a*), we report on the speed of the pair (open diamonds), which is somewhat diminished with respect to the speed of an isolated wing. Here, the gaps in the data indicate that certain intervals of the schooling number S are not accessed by this force perturbation procedure. In general, the pair speed tends to diminish as the two are forced closer together, but the changes in speed are not monotonic and show valleys at the free-swimming equilibria.

https://doi.org/10.1017/jfm.2026.11521 Published online by Cambridge University Press

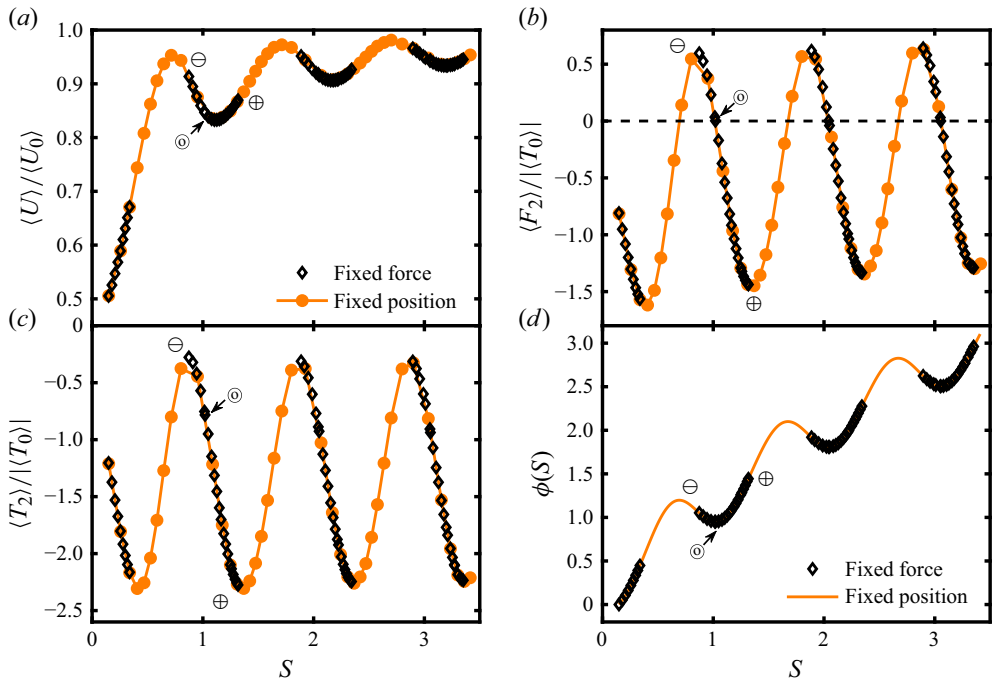


Figure 10. Fixed-force (black open diamonds) and fixed-position (orange symbols and curves) methods for mapping out the interaction of the follower with the leader's wake. The two wings have the same flapping amplitude $\tilde{A} = 0.2$ and the drag coefficient is fixed at $C_f = 0.02$. (*a*) Steady-state speed of the pair normalised by the single-wing speed $\langle U\rangle/\langle U_0\rangle$. (*b*) Total hydrodynamic force on the follower normalised by the single-wing thrust $\langle F_2\rangle/|\langle T_0\rangle|$. (*c*) Thrust on the follower normalised by the single-wing thrust $\langle T_2\rangle/|\langle T_0\rangle|$. (*d*) Hydrodynamic potential for the follower $\phi(S) = -\int\langle F_2\rangle\,\mathrm{d}S$. Three particular cases of fixed-force perturbations correspond to: zero applied force and thus an equilibrium schooling state (◎), a negative applied force that drives the follower closer to the leader (⊖) and a positive force that drives the follower away from the leader (⊕).

More importantly, we observe strong oscillations in the total force and thrust on the follower, as shown in figures 10(*b*) and 10(*c*), respectively. For no applied load $F_{ext} = \langle F_2\rangle = 0$, we recover the equilibrium schooling states with nearly integer values of S, for example the point marked ◎. Near each such state, applying a negative or leftward load on the follower tends to drive it towards the leader – e.g. the point marked ⊖ – which reduces S and which is resisted by a positive $\langle F_2\rangle$. Applying a positive load on the follower tends to drive it away from the leader – e.g. the point marked ⊕ – which increases S and which is resisted by a negative $\langle F_2\rangle$. Thus, the force on the follower due its interaction with the leader's wake is a stabilising one. The data of figure 10(b) also explain why certain ranges of S are not observed. If F_{ext} is made overly large and negative, and thus $\langle F_2\rangle$ large and positive, the follower collides with the leader (i.e. $S \to 0$) rather than settling to a finite S. Likewise, overly large and positive F_{ext} leads to large and negative $\langle F_2\rangle$, and the follower separates from the leader and falls downstream (i.e. $S \to \infty$).

To map out a complete profile of the hydrodynamic restoring force, we use a second method, called the 'ghost follower method', in which the position of the 'ghost' follower in the leader's wake is fixed (figure 9*b*). Specifically, we vary the initial wing separation distance g_0 and prescribe this separation $g(t) = g_0$ throughout the simulation by imposing $U_2(t) = U_1(t)$. Thus, while the leader's dynamics is still determined by force balance and $\langle F_1\rangle = 0$, this is not so for the 'ghost' follower, whose motion would necessitate a

https://doi.org/10.1017/jfm.2026.11521 Published online by Cambridge University Press

time-dependent force with a non-zero average in general, $\langle F_2 \rangle \neq 0$. In our numerical nonlinear solver (§ 2), instead of solving (2.30) for variables X_2 and U_2, we update the position of the follower wing at time t_{n+1} by

$$X_2^{n+1} = X_1^{n+1} + d_0, \quad U_2^{n+1} = U_1^{n+1}, \tag{3.1}$$

where $d_0 = g_0 + c$ is the initial separation distance between the wings. For a given g_0, the system arrives at a new equilibrium, and we measure the stroke-averaged speed $\langle U \rangle$, the total hydrodynamic force $\langle F_2 \rangle$ on the follower and its thrust $\langle T_2 \rangle$, and these data are displayed in figure 10(*a–c*) as the orange dots connected by the orange curve. The results from the two methods are seen to agree well over the intervals of S accessible by both, with slight differences attributable to differences in the swimming motion within the flapping stroke. In addition, this fixed-position method accesses the gaps in the fixed-force method, which correspond to unstable conditions, as argued below.

Analogously to other mechanical systems, the potential experienced by the follower can be defined as the integral of the hydrodynamic force with respect to distance downstream from the leader. In dimensionless form, this hydrodynamic potential is $\phi(S) = -\int \langle F_2 \rangle \, \mathrm{d}S$. In figure 10(*d*) we display as the orange curve the potential as integrated from the data obtained by the fixed-position method and with cubic spline interpolation. The fixed-force method (open diamond symbols) yields a similar profile over the accessible intervals of S. A spline interpolation for the total hydrodynamic force is used to fill in the forbidden gaps and obtain the corresponding potential. Both methods reveal a sloped and corrugated potential (tilted washboard) whose form helps to explain the key results from the simulations. The local minima near integer S are stable wells and correspond to the schooling modes, which may be arrived at by initialising the pair sufficiently close to the associated steady-state separation distance. If initialised at distances corresponding to the peaks, the follower may 'fall' down the potential landscape to the global minimum of $S \approx 0$, explaining the collisions that occur for some values of d_0 (see figure 3*a*). Further, the gaps in the fixed-force method can be seen to correspond to unstable conditions in which the potential has downward concavity, i.e. $\mathrm{d}^2\phi/\mathrm{d}S^2 < 0$.

3.4. *Flow fields and stabilisation mechanism*

To better understand the origin of the stable schooling states, we next compare the flow fields generated by the pair for different applied forces on the follower and thus different interactions with the leader's wake. In figure 11 we show the collective wake structures from simulations corresponding to the three conditions marked in figure 10: decreased separation distance and decreased thrust generated by the follower ($\ominus$); a schooling state equilibrium ($\circledcirc$); and increased separation and increased thrust for the follower ($\oplus$). In this context, increased thrust refers to a more negative thrust, as the propulsive thrust is considered negative due to the wings swimming from right to left. The decreased and increased thrust cases correspond to the ends of the stable branch spanning $S = 1$ in figure 10. In these snapshots of the steady-state or terminal condition, the wings are captured at mid-stroke and flapping downward, and the colour map represents the vertical component of the flow u_y normalised by flapping speed of the wing $V_f = 2\pi A f$. When the follower's thrust reaches its minimum in the direction of swimming ($\ominus$), we find that the follower wing flaps downward in the downward flow of the leader's wake, i.e. the follower's flapping motion is in phase with the wavy wake flow it encounters. This constructive interaction reinforces the flow, leading to a collective wake with large regions of lateral flow. For the maximum thrust case ($\oplus$), however, the follower wing flaps downward in the upward flow of the leader's wake, i.e. the follower's flapping motion is out of phase with

https://doi.org/10.1017/jfm.2026.11521 Published online by Cambridge University Press

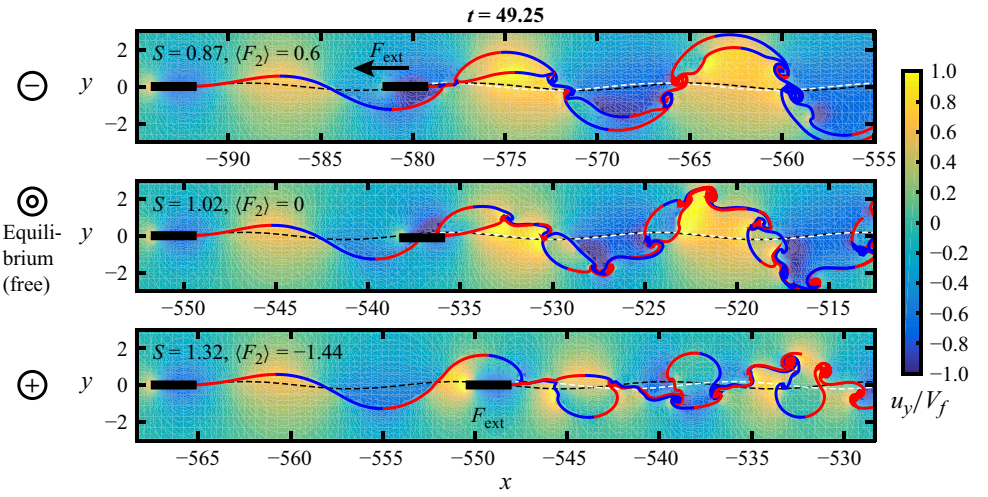


Figure 11. Flow fields for a wing pair with different forces applied to the follower. In this example, the two wings have the same flapping amplitude $\tilde{A} = 0.2$ and the drag coefficient is fixed at $C_f = 0.02$. The snapshots are taken during the middle of the downstroke. Vortex sheets are shed continuously from the trailing edges, with red for positive vortex-sheet strength and blue for negative. The background colour represents the vertical component of flow velocity u_y normalised by wing flapping speed $V_f = 2\pi Af$. Trajectories of leader's trailing edge (black dashed line) and follower's leading edge (white dashed line) are also shown. For the case of minimal thrust generated by the follower (⊖), the follower flaps downward in a downward flow of the leader's wake. For the case of maximal thrust generated by the follower (⊕), the follower flaps downward in an upward flow. For the equilibrium schooling state (◎, $S \approx 1$), the follower spans what would be a node in the leader's wake, with downward flows ahead and upward flows behind.

the leader's wavy wake. This destructive interaction leads to a narrower collective wake with weaker flows. The equilibrium schooling state (◎) is intermediate between these two extremes, with a collective wake that is more similar to that of a single swimmer in its structure and strength.

This flow field characterisation suggests a simple mechanism for the stability of the equilibrium schooling states. A perturbation that decreases the separation distance of the follower from the leader (⊖) leads to reduced thrust since the follower flaps in phase with the flow and thus experiences decreased vertical velocity relative to the fluid. Reduced thrust tends to slow the follower and thus restore it towards the equilibrium schooling state position. A perturbation that increases the separation distance (⊕) leads to increased thrust since the follower flaps out of phase with the flow and thus experiences increased vertical velocity relative to the fluid. Enhanced thrust tends to accelerate the follower towards the leader and again restores the equilibrium schooling state position. Thus it seems the foil–wake interaction can be understood by considering the relative flow during motion through a spatially varying flow field. These results also show that thrust may be enhanced by appropriate positioning within a wake flow, an effect that we exploit in what follows.

3.5. *A 'freeloading' follower with reduced flapping amplitude*

The perturbation studies discussed in § 3.3 show that the follower wing may experience higher or lower thrust depending on its relative position in the wake flow generated by the leader. To explore how wake interactions might be exploited, we consider the case of a 'lazy' and an 'overpowered' follower that flaps at reduced and increased amplitude relative the leader, respectively. In the absence of interactions, reduced amplitude would of course

https://doi.org/10.1017/jfm.2026.11521 Published online by Cambridge University Press

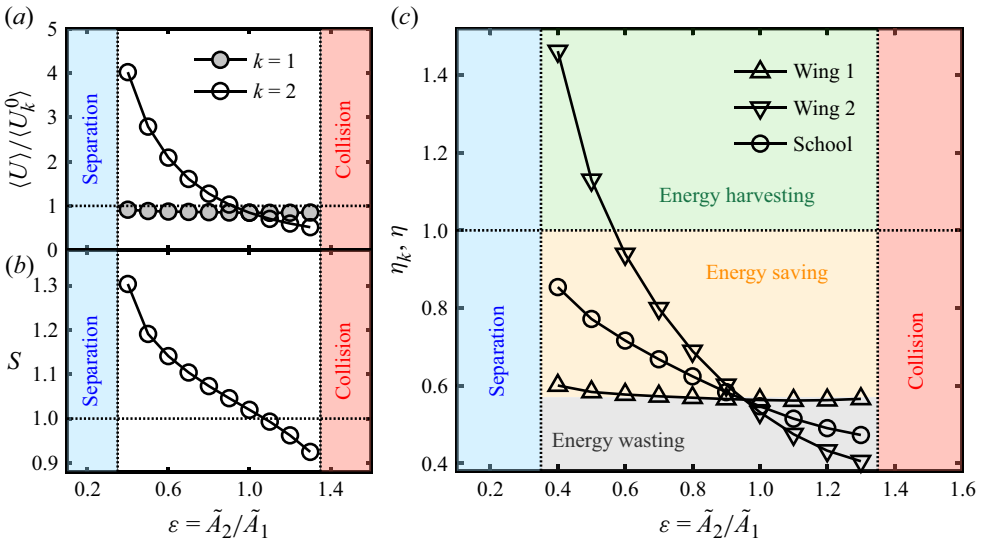


Figure 12. Speed, schooling number and efficiency for a wing pair in which the follower has reduced or increased flapping amplitude relative to the leader. The leader's amplitude is fixed at $\tilde{A}_1 = 0.2$ and the follower's $\tilde{A}_2$ is varied. Steady schooling states near the $S = 1$ branch are found for $\varepsilon = \tilde{A}_2/\tilde{A}_1 \in [0.4, 1.3]$. For $\varepsilon \lesssim 0.4$, the follower can separate from the leader, while for $\varepsilon \lesssim 1.3$, the follower can collide with the leader. (*a*) Swimming speed $\langle U\rangle$ of the pair normalised by the speed of a single wing having the leader's amplitude $\langle U_1^0\rangle$ (grey circles) or follower's amplitude $\langle U_2^0\rangle$ (empty circles). (*b*) First steady schooling state S_1. (*c*) Froude efficiency of the two wings η_1 and η_2, and efficiency of the school η, as given by (2.25). The leader's efficiency is nearly unchanged but the follower experiences a strong increase in efficiency for $\varepsilon < 1$. The follower's efficiency may even exceed unity, indicating that a 'lazy' follower can effectively extract energy from the leader's wake. The school exhibits improved efficiency when $\varepsilon < 1$ but remains below unity, saving energy through flow interactions. An 'overpowered' follower ($\varepsilon > 1$) causes energy to be wasted, as its efficiency falls below the level it would achieve in isolation.

lead to slower swimming (Vandenberghe *et al.* 2004), but low-amplitude swimming in a wake flow presents the opportunity to situate at favourable locations where the follower-flow relative velocity may still be high. To study this 'freeloading' follower problem, we fix the flapping amplitude of the leader wing at $\tilde{A}_1 = 0.2$, vary the follower's amplitude $\tilde{A}_2$, and seek the first steady schooling state near $S = 1$. Fixing $C_f = 0.02$, we find that steady states exist for some initial separation d_0 near the first steady schooling state $S_1 \approx 1$, when $\varepsilon = \tilde{A}_2/\tilde{A}_1 \in [0.4, 1.3]$. In this regime, the two wings 'school' together despite their dissimilar kinematics. For low amplitudes $\varepsilon \lesssim 0.4$, the follower drifts downstream and is unable to generate sufficient thrust to keep pace with the leader, for all initial separations d_0. When $\varepsilon \lesssim 1.3$, the follower generates high thrust that leads to a rear-ending collision with the leader, again for all d_0.

The steady schooling states are characterised by the speed, schooling number, and efficiency plots of figure 12. As the follower's amplitude $\tilde{A}_2$ is varied, we find the school speed $\langle U\rangle$ remains somewhat smaller than the speed $\langle U_1^0\rangle$ of a single wing with the leader's flapping amplitude $\tilde{A}_1$, as shown by the grey circles in figure 12(*a*). However, if the pair speed is compared with a single swimmer of the follower's amplitude $\langle U_2^0\rangle$, we observe a speed enhancement for $\varepsilon < 1$, as shown by the empty circles in figure 12(*a*). This implies that the follower swims at higher speed than it would in isolation, with a speed enhancement of up to four times. This exploitation of the wake flow for $\varepsilon < 1$ is associated

https://doi.org/10.1017/jfm.2026.11521 Published online by Cambridge University Press

with higher schooling numbers S, as shown in figure 12(b). The flow field analysis given above suggests an interpretation of these findings: The weakly flapping follower re-locates to a downstream position in which the wake flow is out of phase with the flapping motion, thereby maintaining strong relative flows and sufficiently high thrust to keep pace with the leader. Increasing ε, which corresponds to an 'overpowered' follower, leads to smaller S. This is explained by the increase in the thrust associated with faster flapping of an isolated single wing, which is counteracted by a compensating decrease in thrust associated with moving closer to the leader, where the follower's upstroke occurs in a stronger upward flow (Newbolt *et al.* 2019).

Finally, we also consider the efficiency of each wing and the pair, as shown in figure 12(c). Because the swimming speed of the pair is nearly unchanged by varying ε, the output power of the leader and follower is nearly unchanged. This leads to little change in the Froude efficiency of the leader. The follower, on the other hand, experiences a strong increase in efficiency for $\varepsilon < 1$ since its input power decreases with decreasing flapping amplitude. The efficiency of the follower may even exceed unity ($\eta_2 > 1$) when $\varepsilon < 0.6$, another manifestation of how wake effects may be exploited. Essentially, a 'lazy' follower can extract more energy from the wake of the leader than it is putting in, getting a 'boost' from the leader's wake. The school also exhibits improved efficiency when $\varepsilon < 1$, although η remains below unity. This indicates that, while the school still performs work when the follower is 'lazy', its overall performance is improved compared with when the wings are operating independently, saving energy through the flow interactions. In contrast, an 'overpowered' follower ($\varepsilon > 1$) may experience reduced efficiency compared with what it could achieve in isolation. In this case, the flow interactions actually lead to wasted energy.

4. Linearised model

To understand the steady schooling of the two wings and the hydrodynamic potential on the follower wing, we adapt a small-amplitude linearised theory (Wu 1961; Wu & Chwang 1975) to our schooling problem of two wings in tandem. The wing is modelled by a flat rigid plate of chord length c, moving with horizontal speed U_∞ (in the negative x-direction) with prescribed vertical motion $h(t) = A\cos(2\pi f t)$, in a 2-D incompressible inviscid fluid. Assuming small flapping amplitude $A/c \ll 1$ and small Strouhal number $St = Af/U_\infty \ll 1$, the 2-D Euler equation as well as the 'no-penetration' boundary condition are linearised and solved at the wing boundary using Fourier series and conformal mapping. The thrust and efficiency can thus be calculated from the solution.

We first adapt the linearised theory developed by Wu (1961) for the swimming of a waving plate with travelling-wave kinematics, to our case of a heaving plate swimming in a quiescent background, by setting the wave amplitude to a constant, and the wavenumber and phase angle to zero. It models the swimming of an isolated single wing, and also serves as a good approximation of the leader wing in the school. This approximation is motivated by experiments (Ramananarivo *et al.* 2016) and our simulations, both of which show the leader wing is affected weakly by the follower, and the school speed differs from the single-wing speed by less than 20 % regardless of the amplitude and location of the follower wing (see figures 6b, 10a and 12a). Combining the thrust formula provided by Wu's solution with the Blasius skin-friction formula (2.8), the free-swimming speed of the single wing, or the leader wing, can be determined.

Under assumptions of small amplitude $A/c \ll 1$ and small Strouhal number $St \ll 1$, the vortex sheet generated by the leader wing can be linearised as a flat vortex sheet, the flow induced by which is then approximated by a simple steady stationary wave. We then examine the interaction of the follower wing with this wave by adapting a similar linearised

https://doi.org/10.1017/jfm.2026.11521 Published online by Cambridge University Press

theory to that of Wu & Chwang (1975), in which a heaving plate in a wavy background stream is solved. Provided by the solution, the thrust of the follower wing can be expressed as a function of the schooling number S. The drag is also provided by the Blasius skin-friction formula (2.8), using the swimming speed as the boundary-layer stream speed, assuming the follower does not feel an extra fluid jet produced by the leader. Combining the thrust and the drag, we can then calculate the hydrodynamic potential on the follower and solve the steady schooling numbers analytically. Recent work (Nitsche *et al.* 2025) has also applied the linear thin-airfoil theory of Wu (1961) to study the dynamics of two or more interacting plates.

4.1. *Linearised model for isolated flapping wings*

4.1.1. *Swimming of a single flapping wing*

We begin by considering a single wing swimming with constant speed U_∞ in a quiescent background. We use the same non-dimensionalisation as in § 2: the characteristic length $\tilde{L} = c/2$, time $\tilde{T} = 1/f$, velocity $\tilde{U} = cf/2$ and pressure $P = \rho_f \tilde{U}^2 = \rho_f c^2 f^2/4$. The heaving motion of the wing described in the body frame is

$$h(x, t) = \tilde{A}\cos(2\pi t), \quad -1 \leqslant x \leqslant 1, \tag{4.1}$$

where the wing spans from $x = -1$ to $x = 1$.

In the frame of the flow, we assume the wing translates with constant velocity $-U_\infty$ in the negative x-direction. Then in the wing frame, the wing is considered to be flapping in a uniform background stream of constant velocity U_∞ in the positive x-direction. Following Wu (1961), the flow velocity is denoted as $\boldsymbol{q} = (U_\infty + u, v)$, where velocity perturbations (u, v) are assumed small compared with the uniform stream U_∞, i.e. $U_\infty \gg u$ and $U_\infty \gg v$. The flow satisfies the 2-D Euler equation, and is linearised as

$$\partial_t \boldsymbol{q} + U_\infty \partial_x \boldsymbol{q} = -\nabla p, \quad \nabla \cdot \boldsymbol{q} = 0. \tag{4.2}$$

The kinematic boundary condition on the wing requires the velocity to be continuous in the normal direction. Assuming the heaving amplitude is small, $\tilde{A} \ll 1$, the boundary condition is then linearised as

$$v(x, y, t)\,|_{y=\pm 0} = \partial_t h(x, t), \quad -1 \leqslant x \leqslant 1. \tag{4.3}$$

Note that in dimensional quantities, (4.3) and condition $U_\infty \gg v$ imply that the Strouhal number $St = Af/U_\infty$ is small, as $U_\infty \gg v \sim Af$, where the Strouhal number denotes the ratio of the vertical flapping speed and the translational speed of the wing.

Instead of solving the fluid velocity directly, Wu (1961) solves for acceleration potential

$$w(z, t) = \phi(x, y, t) + i\psi(x, y, t), \tag{4.4}$$

in complex variables $z = x + iy$. Here,

$$\phi(x, y, t) = -p \tag{4.5}$$

is Prandtl's acceleration potential, which is a harmonic function of (x, y) for every t, and $\psi(x, y, t)$ is its harmonic conjugate. The pressure p is continuous everywhere except across the wing boundary, $-1 \leqslant x \leqslant 1$. It then follows that ϕ is regular inside the flow, so that

$$\phi(x, +0, t) = \phi(x, -0, t), \quad \text{for } |x| > 1, \tag{4.6}$$

https://doi.org/10.1017/jfm.2026.11521 Published online by Cambridge University Press

and for all t. The Kutta condition is required at the trailing edge of the wing

$$|w(1,t)| < \infty, \quad \forall t \geqslant 0. \tag{4.7}$$

Furthermore, far-field boundary conditions

$$w(z,t) \to 0 \quad \text{as} \quad |z| \to \infty; \quad u(z,t) - iv(z,t) \to 0 \quad \text{as} \quad z \to -\infty, \tag{4.8}$$

are required to complete the problem.

Wu (1961) constructed the solution of $w(z,t)$ using Fourier series and conformal transformation. Adjusting this to the pure-heaving plate case considered in this work, simplifies the Fourier series expressions given in Wu (1961). Specifically, all higher Fourier modes vanish, leaving only the uniform mode, and any terms involving $\partial_x h$ are identically zero. Therefore, provided by the solution, the stroke-averaged hydrodynamic thrust on the wing is given as

$$\langle T \rangle = -4\pi^3 \tilde{A}^2 \, |C(\sigma)|^2 \,, \tag{4.9}$$

$$C(\sigma) = \frac{K_1(i\sigma)}{K_0(i\sigma) + K_1(i\sigma)} = C_1(\sigma) + iC_2(\sigma), \quad \sigma = 2\pi/U_\infty, \tag{4.10}$$

where K_0 and K_1 are the modified Bessel functions of the second kind of orders zero and one. The function $C(\sigma)$ is called Theodorsen's function, and $C_1(\sigma)$ and $C_2(\sigma)$ are the real and imaginary parts of $C(\sigma)$, respectively. Using dimensional quantities, $\sigma = \pi cf/U_\infty$ is usually called the reduced frequency. If we consider the problem in the flow frame, that the wing moves with velocity U_∞ in a quiescent background, $\lambda = U_\infty/f$ denotes the wavelength of the wing motion and then $\sigma = \pi c/\lambda$ represents the ratio of the wing size to the wavelength. The thrust (4.9) is in the same direction as swimming (negative x-direction) and is composed of the leading-edge suction only. As discussed in § 2.1 regarding the vortex-sheet model, the pressure distributed along the wing has zero horizontal component, since the body is always horizontally aligned with the flow.

The Froude efficiency (Lighthill 1960), or the stroke-averaged efficiency of propulsion, is defined in the same way as in the vortex-sheet model (§ 2.1), which is provided by Wu (1961) as

$$\eta = \frac{\langle P_{out} \rangle}{\langle P_{in} \rangle} = \frac{|C(\sigma)|^2}{C_1(\sigma)}. \tag{4.11}$$

Here, the output power

$$\langle P_{out}(t) \rangle = \langle T(t) \rangle U_\infty \tag{4.12}$$

is computed from (4.9). The input power required to maintain the flapping motion is expressed as

$$\langle P_{in} \rangle = \left\langle -\int_{-1}^{1} [p] \partial_t h \, \mathrm{d}x \right\rangle; \tag{4.13}$$

calculated by integrating the instantaneous pressure jump distribution $[p](x,t)$ along the wing, where

$$[p](x,t) = p(x,+0,t) - p(x,-0,t), \quad -1 \leqslant x \leqslant 1, \tag{4.14}$$

computed from Wu's solution of $w(z,t)$.

Note that using dimensional quantities, the thrust formula (4.9) is expressed as

$$\langle T \rangle = -2\pi^3 c\rho_f A^2 f^2 \, |C(\sigma)|^2 \,, \quad \sigma = \pi cf/U_\infty, \tag{4.15}$$

https://doi.org/10.1017/jfm.2026.11521 Published online by Cambridge University Press

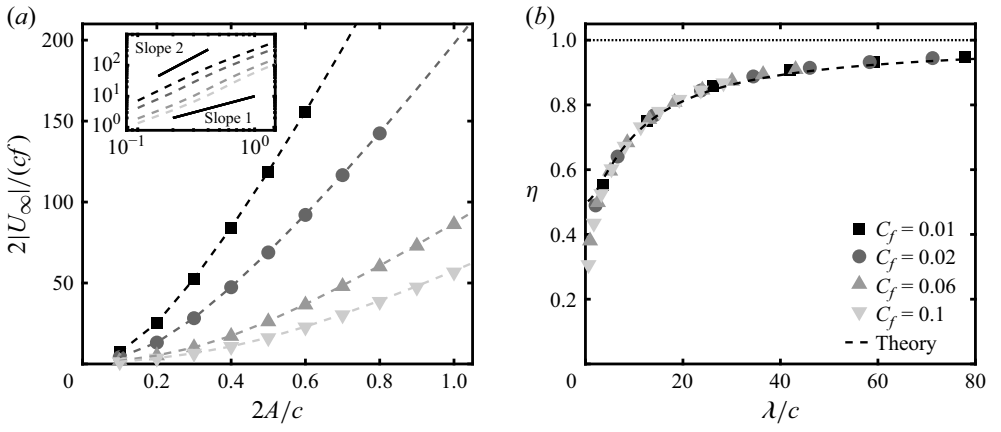


Figure 13. Comparison of linear theory (dashed lines) with simulation (symbols) of single self-propelled flapping wing, for various flapping amplitudes $\tilde{A} = 2A/c$ and drag coefficients C_f. Simulation data are the same as in figure 6. (*a*) Steady swimming speed $|U_\infty|$, normalised by the characteristic speed $cf/2$. The power law of steady speed $2|U_\infty|/(cf)$ in the amplitude $2A/c$ is between linear and quadratic, as shown in the log–log plot in the inset. (*b*) The Froude efficiency η of the single wing at steady state. The linearised theory (4.11) predicts limits of $\eta \to 1$ as $\lambda/c \to +\infty$, and $\eta \to 1/2$ as $\lambda/c \to 0$.

which is quadratic in flapping velocity $V_f = 2\pi Af$ for fixed reduced frequency σ. The limiting case of $\sigma \to 0$ is of particular interest. For small σ, $K_0(i\sigma)$ and $K_1(i\sigma)$ can be expanded as

$$K_0(i\sigma) = -\ln\sigma + \ln 2 - \gamma - i\pi/2 + O(\sigma^2 \ln\sigma), \tag{4.16}$$

$$K_1(i\sigma) = -\frac{\pi}{4}\sigma - \frac{i}{\sigma} + \frac{i\sigma}{4}(2\ln\sigma - 2\ln 2 + 2\gamma - 1) + O(\sigma^3 \ln\sigma), \tag{4.17}$$

where $\gamma \approx 0.5771$ is Euler's constant (Abramowitz & Stegun 1964). Substituting (4.16)–(4.17) in Theodorsen's function (4.10), we obtain $C(\sigma) \to 1$, $C_1(\sigma) \to 1$ as $\sigma \to 0$. Hence $\langle T\rangle \sim -2\pi^3 c\rho_f A^2 f^2$ for small σ, or long free-swimming wavelength $\lambda/c = \pi/\sigma$. The Froude efficiency η in (4.11) is determined only by the reduced frequency σ, and has limit $\eta \to 1$ as $\sigma \to 0$ (see figure 13*b*). In the other limiting case of $\sigma \to +\infty$, we could obtain $C(\sigma) = C_1(\sigma) \to 1/2$, and thus $\langle T\rangle \sim -\pi^3 c\rho_f A^2 f^2$ and $\eta \to 1/2$ for $\sigma \gg 1$. The limit at large σ, or small free-swimming wavelength $\lambda/c = \pi/\sigma$, is not of much interest to free-swimming problems, as the free-swimming speed $U_\infty = \pi cf/\sigma$, determined by the flapping amplitude A and frequency f, does not approach a small value for the parameter ranges of our interest.

For the freely swimming wing, the vertical flapping kinematics determines the free translational speed in the horizontal direction, that is, the free speed U_∞ is a function of the flapping amplitude A and frequency f. The steady free speed U_∞ can be solved from balancing the thrust and drag. The thrust $\langle T\rangle$ is provided by (4.9) (dimensionless), or (4.15) (dimensional). The drag D is modelled using a simplification of the skin-friction model (2.13) used in simulations, where the boundary-layer velocity is approximated using the free-swimming velocity of the wing

$$D = 2C_f |U_\infty|^{3/2}, \tag{4.18}$$

and the drag coefficient C_f is provided by (2.14). The dimensionless free-swimming speed U_∞ is then solved from balance of forces

$$0 = \langle T\rangle + D = -4\pi^3 \tilde{A}^2 |C(\sigma)|^2 + 2C_f |U_\infty|^{3/2}, \quad \sigma = 2\pi/U_\infty. \tag{4.19}$$

https://doi.org/10.1017/jfm.2026.11521 Published online by Cambridge University Press

The steady swimming speed U_∞, solved from (4.19), is shown in figure 13(*a*), compared with the steady speed of a single flapping wing calculated through the vortex-sheet simulations (see figure 6*a*). Figure 13(*b*) compares the Froude efficiency of the single wing at steady swimming state, calculated using vortex-sheet simulation and the linearised theory (4.11). The results from linearised theory agree well with the simulation results. For the parameter values used in our simulations, the flapping amplitude ($A/c = 0.05$ to 0.5) and the Strouhal number ($St \approx 0.005$ to 0.1) are within small ranges, so the linearisation provides a good approximation. The log–log plot of the free speed, in the inset of figure 13(*a*), shows that the free speed U_∞ is superlinear in flapping amplitude, which agrees with the power law in experiments. This will be discussed further in § 5.

4.1.2. *Fluid wake generated by single flapping wing*

The vortex wake generated by a flapping wing is complex and self-developing, as shown by our simulation figure 11 and by experimental flow visualisations (Vandenberghe *et al.* 2006; Ramananarivo *et al.* 2016). In the linear regime, the Strouhal number $St = Af/U_\infty$, the ratio of the vortex wake width A and wavelength $\lambda = U_\infty/f$, is assumed to be small. The vortex sheet, shed tangentially from the trailing edge (by the Kutta condition; see Jones (2003)), is assumed to lie along the x-axis downstream of the wing trailing edge (as in the schematic diagram in figure 14). We define the vortex-sheet strength $\gamma(x, t)$ at point $(x, 0)$ as

$$\gamma(x, t) = u(x, +0, t) - u(x, -0, t). \tag{4.20}$$

We consider the vortex sheet in the wing frame; the sheet defined on $x \geqslant 1$ downstream the wing trailing edge ($x = 1$). According to (4.2) and (4.6), the vortex-sheet strength γ satisfies

$$\partial_t \gamma + U_\infty \partial_x \gamma = 0, \quad x \geqslant 1, \tag{4.21}$$

which shows that γ is dependent only on a single variable $(x - U_\infty t)$, and

$$\gamma(x, t) = \gamma\left(1, t - \frac{(x-1)}{U_\infty}\right). \tag{4.22}$$

The vortex-sheet strength at the trailing edge is calculated by Wu (1961) as

$$\gamma(1, t) = \frac{4\pi^2 \tilde{A}}{G(\sigma)} \sin\left(2\pi\left(t - \frac{\sigma}{2\pi} - g(\sigma)\right)\right), \quad \sigma = 2\pi/U_\infty, \tag{4.23}$$

$$\mathcal{G}(\sigma) = K_0(i\sigma) + K_1(i\sigma) = G(\sigma) e^{2\pi i g(\sigma)}, \tag{4.24}$$

where $G(\sigma)$ and $g(\sigma)$ are the modulus and angle of $\mathcal{G}(\sigma)$, respectively. Substituting (4.23) in (4.22), the vortex-sheet strength is then provided as

$$\gamma(x, t) = \frac{4\pi^2 \tilde{A}}{G(\sigma)} \sin\left(2\pi\left(t - \frac{\sigma x}{2\pi} - g(\sigma)\right)\right), \quad \sigma = 2\pi/U_\infty, \tag{4.25}$$

where $x \geqslant 1$ denotes the downstream of the wing trailing edge.

Now we change back to the flow frame, where the wing swims with speed $-U_\infty$ towards the negative x-direction in a quiescent environment. The flow frame variables $(\tilde{x}, \tilde{y}, \tilde{t})$ and the wing frame variables (x, y, t) are related through

$$(\tilde{x}, \tilde{y}, \tilde{t}) = (x - U_\infty t, y, t). \tag{4.26}$$

https://doi.org/10.1017/jfm.2026.11521 Published online by Cambridge University Press

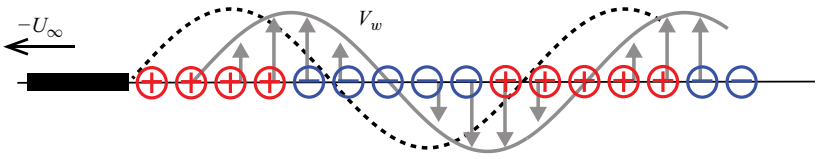


Figure 14. The vortex sheet generated by a single flapping wing with swimming velocity $-U_\infty$ (in the negative x-direction) is assumed to lie along the x-axis downstream of the wing. It has δ_1 phase lag from the wing trailing-edge trajectory (dashed line). The wake induced by the flat vortex sheet can be approximated by a steady stationary wave V_w, which has δ_2 phase lag from the wing trailing-edge trajectory. See (4.29) and (4.37). The red $\oplus$ denote positive vorticity and the blue $\ominus$ denote negative vorticity.

The position of the wing trailing edge $(\tilde{x}_b, \tilde{y}_b)$ in the flow frame can be parameterised in $\tilde{t}$ as

$$\tilde{x}_b = -U_\infty \tilde{t} + 1, \quad \tilde{y}_b = \tilde{A}\cos\left(2\pi\tilde{t}\right), \tag{4.27}$$

from which the trajectory of the trailing edge is thus provided as

$$\tilde{y}_b(\tilde{x}) = \tilde{A}\cos\left(2\pi\frac{(1-\tilde{x})}{U_\infty}\right) = \tilde{A}\cos\left(2\pi\frac{(\tilde{x}-1)}{\lambda}\right). \tag{4.28}$$

Here, the wavelength of the motion is $\lambda = U_\infty = 2\pi/\sigma$ using dimensionless variables. Substituting (4.26) in (4.25), we obtain that the vortex-sheet strength in the flow frame is given by

$$\gamma(\tilde{x}) = -\frac{4\pi^2\tilde{A}}{G(\sigma)}\sin\left(2\pi\left(\frac{\tilde{x}}{\lambda} + g(\sigma)\right)\right), \quad \tilde{x} \geqslant \tilde{x}_b, \tag{4.29}$$

where $\tilde{x}_b = -U_\infty\tilde{t} + 1$ denotes the location of the wing trailing edge.

We note that the vortex-sheet strength (4.29) has a phase lag of δ_1 from the trailing-edge trajectory (4.28), where

$$\delta_1(\sigma) = -1/4 - g(\sigma) - \sigma/(2\pi). \tag{4.30}$$

In the limiting case of $\sigma \to 0$, we obtain

$$G(\sigma) \to \infty, \ g(\sigma) \to -1/4, \tag{4.31}$$

using (4.16)–(4.17) and (4.24). Substituting (4.31) in (4.29)–(4.30), it then follows that the magnitude of the vortex-sheet strength $\gamma_0 = 4\pi^2\tilde{A}/G(\sigma) \to 0$, and the phase lag $\delta_1(\sigma) \to 0$ as $\sigma \to 0$. These limits indicate a weak vortex-sheet wake when the wavelength λ, or the swimming speed U_∞ is large. Moreover, the vorticity shed by the trailing edge is nearly in phase with the motion of the trailing edge, in the regime of large λ or U_∞. This agrees with experimental flow visualisations in Ramananarivo *et al.* (2016), which show that vortex cores are roughly located at the peak of the trailing-edge trajectory. The limit of $\sigma \to +\infty$ is of less interest as the steady speed of free swimming U_∞ does not achieve small values for the parameter values of our interest. For the range $U_\infty \in [2, \infty)$ (i.e. $\sigma \in (0, \pi]$), which covers the range of U_∞ in our simulations, we compute numerical ranges $0 < 1/G(\sigma) \lesssim 0.705$, and $-0.12 \lesssim \delta_1(\sigma) < 0$ which indicates that the phase-lag δ_1 between the trailing-edge trajectory and the vorticity is always less than a quarter.

The fluid velocity induced by the vortex sheet (4.29) can be calculated through the Biot–Savart law. To calculate the flow velocity on the x-axis downstream the wing (or the mean velocity at the vortex sheet), we ignore the circulation on the wing body, and approximate

https://doi.org/10.1017/jfm.2026.11521 Published online by Cambridge University Press

the flow field using that induced by the vortex sheet, provided as

$$u(\tilde{x},0,t)-iv(\tilde{x},0,t)=\frac{1}{2\pi i}\int_{\tilde{x}_b}^{\infty}\frac{\gamma(\tilde{x}')}{\tilde{x}-\tilde{x}'}\,\mathrm{d}\tilde{x}',\quad \tilde{x}\geqslant\tilde{x}_b, \tag{4.32}$$

where $\tilde{x}_b$ denotes the location of the wing trailing edge. Note that $u(\tilde{x},0,t)=0$, as the right-hand side of (4.32) is purely imaginary. While the horizontal velocity on the x-axis, downstream the wing, is zero, the vertical velocity is given by

$$\begin{aligned}v(\tilde{x},0,t)&=\frac{1}{2\pi}\int_{\tilde{x}_b}^{+\infty}\frac{\gamma(\tilde{x}')}{\tilde{x}-\tilde{x}'}\,\mathrm{d}\tilde{x}'\\&=-\frac{2\pi\tilde{A}}{G(\sigma)}\int_{\tilde{x}_b}^{+\infty}\frac{\sin\left(2\pi(\tilde{x}/\lambda+g(\sigma))\right)}{\tilde{x}-\tilde{x}'}\,\mathrm{d}\tilde{x}'\\&=\frac{2\pi^2\tilde{A}}{G(\sigma)}\left\{\cos\left(2\pi\left(\frac{\tilde{x}}{\lambda}+g(\sigma)\right)\right)+J(\tilde{x},\tilde{x}_b)\right\},\end{aligned} \tag{4.33}$$

$$\begin{aligned}J(\tilde{x},\tilde{x}_b)=\frac{1}{\pi}\Bigg[&\left(\mathrm{Si}(2\pi(\tilde{x}-\tilde{x}_b)/\lambda)-\frac{1}{2}\pi\right)\cos\left(2\pi(\tilde{x}/\lambda+g(\sigma))\right)\\&-\mathrm{Ci}(2\pi(\tilde{x}-\tilde{x}_b)/\lambda)\sin\left(2\pi(\tilde{x}/\lambda+g(\sigma))\right)\Bigg],\quad \tilde{x}\geqslant\tilde{x}_b,\end{aligned} \tag{4.34}$$

where $\mathrm{Si}(x)=\int_0^x(\sin t/t)\,\mathrm{d}t$ and $\mathrm{Ci}(x)=-\int_x^{+\infty}(\cos t/t)\,\mathrm{d}t$ are the sine integral and cosine integral of real arguments, respectively.

Note that (4.34) can be bounded by its magnitude function $I(\tilde{x}-\tilde{x}_b)$, where

$$I(x)=\sqrt{\left(\mathrm{Si}(2\pi x)-\frac{1}{2}\pi\right)^2+\mathrm{Ci}^2(2\pi x)}. \tag{4.35}$$

It is easy to show that $I(x)$ is a monotonically decreasing function. For location $\tilde{x}$ that is at least one wavelength away from the wing trailing edge $\tilde{x}_b$, i.e. $(\tilde{x}-\tilde{x}_b)/\lambda\geqslant 1$, (4.34) is bounded numerically, as follows:

$$|J(\tilde{x},\tilde{x}_b)|\leqslant\frac{1}{\pi}I((\tilde{x}-\tilde{x}_b)/\lambda))\leqslant I(1)\approx 0.05. \tag{4.36}$$

In (4.33), the magnitude of $J(\tilde{x},\tilde{x}_b)$ is small compared with $\cos(2\pi(\tilde{x}/\lambda+g))$, the other term in the bracket. Therefore, $J(\tilde{x},\tilde{x}_b)$ can be neglected and (4.33) can be approximated in a simple wave form (figure 14), as

$$v(\tilde{x},0,t)\approx V_w(\tilde{x})=\frac{2\pi^2\tilde{A}}{G(\sigma)}\cos\left(2\pi\left(\frac{\tilde{x}}{\lambda}+g(\sigma)\right)\right). \tag{4.37}$$

Moreover, for large x, the asymptotic expansion $I(x)=1/(2\pi^2x)+O(x^{-3})$ is obtained from expansions of $\mathrm{Si}(x)$ and $\mathrm{Ci}(x)$. It then follows that $|J(\tilde{x},\tilde{x}_b)|\to 0$ for $(\tilde{x}-\tilde{x}_b)/\lambda\to+\infty$, which indicates that the approximation $V_w(\tilde{x})$ in (4.37) is closer to $v(\tilde{x},0,t)$ for $\tilde{x}$ further away the wing trailing edge $\tilde{x}_b$. Note that the wave $V_w(\tilde{x})$ (4.37) is a quarter lag in phase from the vorticity distribution $\gamma(\tilde{x})$ (4.29). Therefore, the phase difference between the wave $V_w(\tilde{x})$ and the trailing-edge trajectory $\tilde{y}_b(\tilde{x})$ (4.28) is then

$$\delta_2(\sigma)=\delta_1(\sigma)+1/4=-g(\sigma)-\frac{\sigma}{2\pi}, \tag{4.38}$$

and it has the limit $\delta_2(\sigma)\to 1/4$ as $\sigma\to 0$.

https://doi.org/10.1017/jfm.2026.11521 Published online by Cambridge University Press

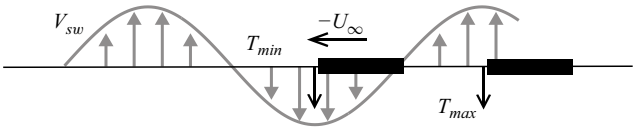


Figure 15. A single flapping wing swimming with velocity $-U_\infty$ (negative x-direction) interacts with a stationary wave V_{sw} in the background. When the leading-edge velocity of the wing is in phase with the wave, the effective wing flapping is reduced and the wing thrust reaches a minimum value T_{min}. When the wing leading edge is out of phase with the wave, the effective flapping speed is increased and the thrust reaches a maximum value T_{max}.

The steady stationary wave $V_w(\tilde{x})$ in (4.37) provides a simple model of the flow at the centreline of a reverse von Kármán vortex street, in the limit of small Strouhal number $St = Af/U_\infty$. For the parameters used in both the schooling experiments and our simulations, the flapping velocity $V_f = 2\pi Af$ is small compared with the swimming velocity U_∞ so that the Strouhal number is small. In the experiments of Ramananarivo *et al.* (2016), $St = 0.1$ to 0.2, and in our simulations $St = 0.005$ to 0.1. From experimental flow visualisation of a single flapping wing (Becker *et al.* 2015; Ramananarivo *et al.* 2016) and our simulations (see the wake of the leader wing in figure 11), we find that the backward jet flow at the centreline in the reverse von Kármán street is weak, as the Strouhal number is small. Flow visualisation shows alternating upward and downward flow jets along the centreline of the wake generated by a single flapping wing. This allows us to use a waveform (4.37) to model the flow at the centreline of the wake produced by the leader wing in the school, and subsequently study its interaction with the follower wing.

4.1.3. *Single flapping wing interacting with steady wave*

Now we consider a single flapping wing interacting with a wavy stream in the background (figure 15). It serves as a model for the follower swimmer in the 'school-of-two', that is surrounded by the wake produced by the leader wing. In the frame of the wing, where the wing spans in the range $-1 \leqslant x \leqslant 1$, we assume the wing is immersed in a wavy stream with velocity $(U_\infty, V_{sw}(x, t))$. The x-component of this background flow is a uniform stream U_∞, and the y-component V_{sw} is a travelling wave of the same velocity U_∞ and the frequency is f, the same frequency as the flapping wing. We denote the wavelength by $\lambda = U_\infty/f$. Using dimensionless variables, where $f = 1$, the travelling wave is given by

$$V_{sw}(x, t) = V_0 \sin(2\pi(x/\lambda - t)), \quad \lambda = U_\infty/f, \tag{4.39}$$

where V_0 is the amplitude of the wave, and the heaving motion of the wing has the form

$$h(x, t) = \tilde{A} \cos(2\pi(t + \theta)), \quad -1 \leqslant x \leqslant 1, \tag{4.40}$$

where θ is a phase shift in time, and the flapping frequency ($f = 1$) is the same as the travelling wave.

The linearised problem of a rigid wing flapping in a wavy stream is solved by Wu & Chwang (1975). There, the wing maintains a superposition motion of pitching and heaving, with the flapping frequency required to be the same as the frequency of the wavy stream. In this work, we adapt the calculation of Wu & Chwang (1975) to our case of a purely heaving wing (4.40), flapping in a wavy stream (U_∞, V_{sw}) with the wave speed the same as the stream speed.

We assume the heaving amplitude $\tilde{A}$ and the amplitude of the wave V_0 are small, and denote $\epsilon = V_0/(2\pi\tilde{A}) = O(1)$ (using dimensionless variables; $\epsilon = V_0/(2\pi Af)$ if using dimensional variables) the ratio of the wave velocity to the flapping velocity. Similar to

https://doi.org/10.1017/jfm.2026.11521 Published online by Cambridge University Press

the linearisation of a single wing in a quiescent background (see § 4.1.1), we denote the flow velocity by $\boldsymbol{q} = (U_\infty + u,\, V_{sw} + v)$. Assuming $U_\infty \gg u$ and $U_\infty \gg v$, the linearised 2-D Euler (4.2) has the following kinematic boundary condition:

$$v_1(x,\, y,\, t)\,|_{y=\pm 0} = \partial_t h(x,\, t) - V_{sw}(x,\, t), \quad -1 \leqslant x \leqslant 1. \tag{4.41}$$

Using the same assumptions (4.6)–(4.8) in § 4.1.1, the acceleration potential $w(z,\, t)$ (defined in (4.4)) is solved by Wu & Chwang (1975) through Fourier series analysis and conformal mapping techniques, a process similar to that in Wu (1961). The stroke-averaged thrust on the wing is provided by Wu & Chwang (1975) as

$$\langle T\rangle = -4\pi^3 \tilde{A}^2\,|C(\sigma)|^2 \left[1 + \epsilon^2 P^2(\sigma) + 2\epsilon P(\sigma)\sin(2\pi\,(\theta - p(\sigma)))\right], \tag{4.42}$$

$$\mathcal{P}(\sigma) = \frac{\overline{K_1(i\sigma)}K_0(i\sigma) + \overline{K_0(i\sigma)}K_1(i\sigma)}{\pi K_1(i\sigma)} = P(\sigma)e^{2\pi i p(\sigma)}, \tag{4.43}$$

where $\epsilon = V_0/(2\pi\tilde{A})$, $\sigma = 2\pi/U_\infty$, $P(\sigma)$ and $p(\sigma)$ are the modulus and angle of $\mathcal{P}(\sigma)$, respectively. Note that the thrust (4.42) has a simple sinusoidal form of three variables θ, ϵ and σ, where θ denotes the phase difference between the wave and the wing flapping, ϵ denotes the ratio of the flapping speed and the wave speed and $\sigma = 2\pi/U_\infty = 2\pi/\lambda$ ($\sigma = \pi c f/U_\infty = \pi c/\lambda$ using dimensional quantities) represents the wavelength λ of the wave, or stream speed U_∞.

In the flow frame, where the x-component of the background flow is zero and the wing translates with velocity $-U_\infty$ in the negative x-direction, by substituting (4.26) in (4.39), the background wave (4.39) now becomes a steady vertical wave

$$\tilde{V}_{sw}(\tilde{x}) = V_0 \sin(2\pi\tilde{x}/\lambda). \tag{4.44}$$

The leading edge of the wing, parameterised in $\tilde{t}$ as

$$\tilde{x} = -U_\infty \tilde{t} - 1, \quad \tilde{y} = \tilde{A}\cos(2\pi(\tilde{t} + \theta)), \tag{4.45}$$

follows the trajectory

$$\tilde{y}(\tilde{x}) = \tilde{A}\cos(2\pi\,((\tilde{x} + 1)/\lambda - \theta)). \tag{4.46}$$

Using (4.46) and (4.44), we obtain the phase lag of the wing's leading edge $\tilde{y}(\tilde{x})$ to the vertical wave $\tilde{V}_{sw}(\tilde{x})$, that is,

$$\tilde{\theta} = \theta - \sigma/(2\pi) - 1/4, \tag{4.47}$$

where $\sigma = 2\pi/\lambda$, and the thrust on the wing (4.42) can be expressed in terms of $\tilde{\theta}$ as

$$\langle T\rangle = -4\pi^3 \tilde{A}^2\,|C(\sigma)|^2 \left[1 + \epsilon^2 P^2(\sigma) + 2\epsilon P(\sigma)\cos\left(2\pi\,\left(\tilde{\theta} - \delta_3(\sigma)\right)\right)\right], \tag{4.48}$$

$$\delta_3(\sigma) = p(\sigma) - \sigma/(2\pi). \tag{4.49}$$

It is shown by (4.48) that the extrema of $\langle T\rangle$ are determined by the phase difference between the wing and the wave $\tilde{\theta}$, which is of particular interest. Extreme values of thrust $\langle T\rangle$ are

$$\langle T\rangle_{max} = -4\pi^3 \tilde{A}^2\,|C(\sigma)|^2\,[1 + \epsilon P(\sigma)]^2, \quad \text{when} \quad \tilde{\theta} = \delta_3 + k, \tag{4.50}$$

$$\langle T\rangle_{min} = -4\pi^3 \tilde{A}^2\,|C(\sigma)|^2\,[1 - \epsilon P(\sigma)]^2, \quad \text{when} \quad \tilde{\theta} = \delta_3 + k + 1/2, \tag{4.51}$$

where $k \in \mathbb{Z}^+$. For $\lambda \in [2,\, \infty)$, i.e. $\sigma = 2\pi/\lambda \in (0,\, \pi]$, which is the main range of interest, the numerical value is approximately $0.143 \lesssim \delta_3 \leqslant 1/4$, which is approximately a quarter.

https://doi.org/10.1017/jfm.2026.11521 Published online by Cambridge University Press

Moreover, in the limit of $\sigma \to 0$, we obtain $P(\sigma) \to 1$ and $p(\sigma) \to 1/4$ by substituting asymptotic expansions of the modified Bessel functions (4.16)–(4.17) in (4.43), and thus $\delta_3(\sigma) \to 1/4$. These values indicate that the maximum thrust is achieved when the wing leading-edge trajectory (4.46) has phase-lag $\tilde{\theta} \approx k + 1/4$ to the stationary wave (4.44), and the minimum thrust is achieved when the leading-edge trajectory has about $\tilde{\theta} \approx k + 3/4$ phase lag to the wave.

This could be explained by looking at the flapping velocity of the wing leading edge, which can be parameterised as

$$\tilde{x} = -U_\infty \tilde{t} - 1, \quad \dot{\tilde{y}} = -2\pi \tilde{A} \sin(2\pi(\tilde{t} + \theta)), \tag{4.52}$$

by (4.26), and be expressed in $\tilde{x}$ as

$$\dot{\tilde{y}}(\tilde{x}) = 2\pi \tilde{A} \sin\left(2\pi\left(\tilde{x}/\lambda - \tilde{\theta} - 1/4\right)\right). \tag{4.53}$$

We define an 'effective flapping' velocity at the wing leading edge

$$V_{eff}(\tilde{x}) = \dot{\tilde{y}}(\tilde{x}) - \tilde{V}_{sw}(\tilde{x}) = 2\pi \tilde{A} \sin\left(2\pi\left(\tilde{x}/\lambda - \tilde{\theta} - 1/4\right)\right) - V_0 \sin(2\pi\tilde{x}/\lambda), \tag{4.54}$$

which is the relative velocity of the wing flapping (4.53) and the background wave (4.44). Note that the maximum thrust (4.50) is achieved when $\tilde{\theta} \approx k + 1/4$, at which time the flapping velocity of the leading edge (4.53) is out of phase with the wave, and the effective flapping has a maximum amplitude

$$V_{eff,max}(\tilde{x}) = (2\pi \tilde{A} + V_0) \sin(2\pi\tilde{x}/\lambda), \tag{4.55}$$

as shown in the schematic diagram in figure 15. Similarly, the minimum thrust corresponds to the heaving velocity at the leading edge in phase with the wave, and the amplitude of effective flapping achieves minimum

$$V_{eff,min}(\tilde{x}) = (2\pi \tilde{A} - V_0) \sin(2\pi\tilde{x}/\lambda). \tag{4.56}$$

These results are not surprising. As the thrust $\langle T \rangle$ consists only of the suction force at the leading edge of the wing, when the background wave is out of phase with the flapping velocity of the wing leading edge, the effective flapping is increased and the wing thrust is thus increased and reaches a maximum. Similarly when the wave is in phase with the flapping of the wing leading edge, the effective flapping is decreased and the thrust reaches a minimum.

4.2. *Linearised theory adapted to two wings in tandem*

Now we adapt the linearised calculation on individual wings to the school of two wings swimming in tandem. The two wings are assumed to have the same swimming velocity $-U_\infty$ in the negative x-direction, while the leader wing has flapping amplitude $\tilde{A}_1$ and the follower has amplitude $\tilde{A}_2$ (see schematics in figure 16). To adapt the linearised theory to schooling, we approximate the leader wing using calculations of an isolated single wing, assuming the leader maintains a constant motion and neglecting the hydrodynamic perturbation induced by the follower to the leader. This is motivated by previous simulation results (§ 3) that the speed of the leader wing stays always close to the speed of single wing for the follower not following closely (schooling number S not too small), regardless of the location and flapping amplitude of the follower wing (see figures 6*b* and 10*a*). It is also supported by the experiments of Ramananarivo *et al.* (2016), which show that the schooling speed is always close to the single-wing speed, with a difference of about 10 % for most cases. The wake generated by the leader wing is approximated by a spatial wave of amplitude $V_0 = 2\pi^2 \tilde{A}_1 / G(\sigma)$ and phase-lag $\delta_2(\sigma)$ to the wing trailing edge, where

https://doi.org/10.1017/jfm.2026.11521 Published online by Cambridge University Press

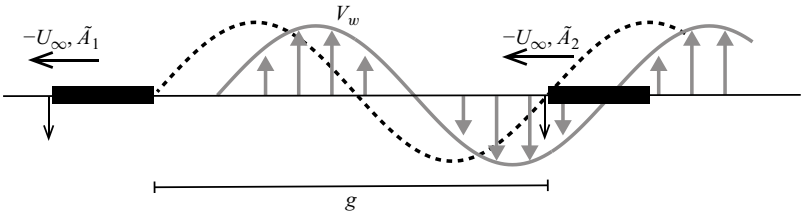


Figure 16. Adapted linearised theory to schooling of two wings in tandem. The wings flap with amplitude $\tilde{A}_1$ and $\tilde{A}_2$, respectively, and swim with the same velocity $-U_\infty$ in the negative x-direction. The leader generates a spatial wave V_w which produces a hydrodynamic potential on the follower. The dashed line denotes the trailing-edge trajectory of the leader wing. The 'tail-head' separation between the wings is denoted by g.

$\sigma = 2\pi/U_\infty$ ((4.37) and (4.38)). We calculate the hydrodynamic potential that the leader induces on the follower by considering the interaction of the follower with this stationary wave, neglecting perturbations due to the body of the leader wing.

4.2.1. *Hydrodynamic thrust of the follower wing*

We denote the distance between the follower's head and the leader's tail by g (as in figure 16). The schooling number defined as $S = g/\lambda$ ($\lambda = U_\infty/f$) denotes the phase lag of the follower's head to leader's tail, following which the phase lag of the follower's leading edge to the stationary wave generated by the leader is

$$\tilde{\theta} = S - \delta_2(\sigma). \tag{4.57}$$

Substituting (4.57) in (4.48), and by (4.24), (4.38), (4.43) and (4.49), we express the thrust on the follower in schooling number S as

$$\langle T_2\rangle = \langle T_1\rangle \left[\varepsilon^2 + Q^2(\sigma) + 2\varepsilon\, Q(\sigma)\cos\left(2\pi\,(S - \delta_4(\sigma))\right)\right], \quad \varepsilon = \tilde{A}_2/\tilde{A}_1, \tag{4.58}$$

$$\delta_4(\sigma) = \delta_2(\sigma) + \delta_3(\sigma) = q(\sigma) - \sigma/\pi, \tag{4.59}$$

where $\langle T_1\rangle = -4\pi^3\tilde{A}_1^2\,|C(\sigma)|^2$ is the thrust of the leader wing (4.9), $Q(\sigma)$ and $q(\sigma)$ are the modulus and angle of

$$\mathcal{Q}(\sigma) = \frac{\pi\mathcal{P}(\sigma)}{\mathcal{G}(\sigma)} = \frac{\overline{K_1(i\sigma)}K_0(i\sigma) + \overline{K_0(i\sigma)}K_1(i\sigma)}{K_1(i\sigma)\,[K_0(i\sigma) + K_1(i\sigma)]} = Q(\sigma)e^{2\pi i q(\sigma)}, \tag{4.60}$$

respectively. In figure 17(*a*), the follower's thrust (black solid curve) calculated from (4.58) is compared with the thrust computed by the vortex-sheet simulations (grey solid curve) in § 3, in which the thrust is measured on a 'ghost follower' maintaining a fixed separation to the leader. Here, the two wings have the same amplitude $\tilde{A} = 0.2$, the drag coefficient is fixed at $C_f = 0.02$ and σ in (4.58) is calculated from (4.19).

Note that the follower's thrust (4.58) is a sinusoidal function in schooling number S, i.e. it depends on the phase difference between the two wings swimming. The coefficients of this sinusoidal function depend on the amplitude ratio of the wings $\varepsilon = \tilde{A}_2/\tilde{A}_1$ and the wavelength of the motion $\lambda/c = 2\pi/\sigma$ (dimensionless). For $\varepsilon = 0$, (4.58) simplifies to

$$\langle T_2\rangle|_{\varepsilon=0} = \langle T_1\rangle\, Q^2(\sigma) = -4\pi^3\,|C(\sigma)|^2\left(Q(\sigma)\tilde{A}_1\right)^2. \tag{4.61}$$

This implies that when the follower wing is a non-flapping 'dead wing', if it somehow still maintains a swimming speed U_∞, it can generate a non-zero constant thrust due to the

https://doi.org/10.1017/jfm.2026.11521 Published online by Cambridge University Press

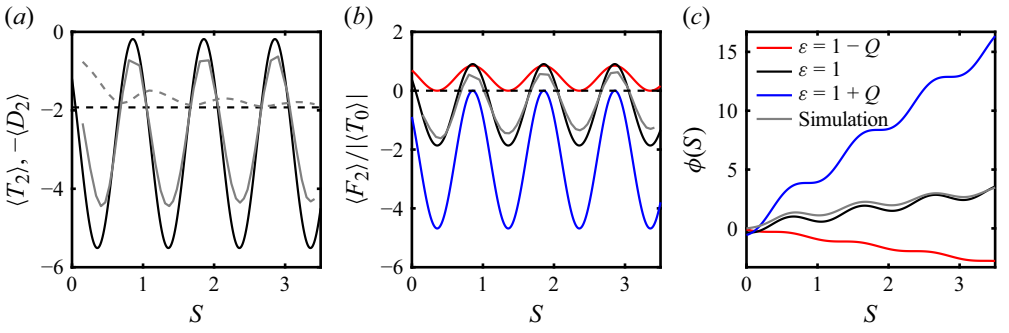


Figure 17. Comparisons between the hydrodynamic forces and potential on the follower wing calculated from linearised theory (black) and from simulations (grey). (*a*) Hydrodynamic thrust $\langle T_2\rangle$ (solid lines) and drag $-\langle D_2\rangle$ (dashed lines) as functions of schooling number S, where the two wings have the same flapping amplitude $\tilde{A} = 0.2$. The forces here are dimensionless. (*b*) Total hydrodynamic force on the follower $\langle F_2\rangle$ normalised by the single-wing thrust $|\langle T_0\rangle|$. (*c*) Hydrodynamic potential on the follower. In (*b*)–(*c*), the leader's amplitude is fixed at $\tilde{A}_1 = 0.2$, while the follower's amplitude $\tilde{A}_2$ is varied. Here, $\varepsilon = \tilde{A}_2/\tilde{A}_1 = 1 - Q$ (red), 1 (black and grey), and $1 + Q$ (blue). In all cases the drag coefficient is $C_f = 0.02$.

interaction with the wavy wake shed by the leader. This 'dead-follower' thrust $\langle T_2\rangle|_{\varepsilon=0} \to 0$ at the long wavelength limit $\sigma \to 0$, as $Q(\sigma) \to 0$ ((4.16)–(4.17) and (4.60)).

The follower's thrust (4.58) achieves extreme values

$$\langle T_2\rangle_{max} = \langle T_1\rangle\,[\varepsilon + Q(\sigma)]^2 = -4\pi^3\,|C(\sigma)|^2\left[\tilde{A}_2 + Q(\sigma)\tilde{A}_1\right]^2,\ \text{when } S = \delta_4 + k,$$
$$\langle T_2\rangle_{min} = \langle T_1\rangle\,[\varepsilon - Q(\sigma)]^2 = -4\pi^3\,|C(\sigma)|^2\left[\tilde{A}_2 - Q(\sigma)\tilde{A}_1\right]^2,\ \text{when } S = \delta_4 + k + 1/2, \tag{4.62}$$

where $k \in \mathbb{Z}^+$. In the limiting case of $\sigma \to 0$, we have $q(\sigma) \to 1/2$ and thus $\delta_4 \to 1/2$ (4.59). This implies that at the long wavelength limit, $\lambda/c \to \infty$, the maximum thrust $\langle T_2\rangle_{max}$ is achieved when the schooling number $S \approx 1/2 + k$ and minimum thrust $\langle T_2\rangle_{max}$ occurs at $S \approx k$. Moreover, we note that the perturbation due to the schooling is weak as $Q(\sigma) \to 0$ when $\sigma \to 0$. When $\sigma = 0$, the follower's thrust $\langle T_2\rangle = -4\pi^3\tilde{A}_2^2|C(\sigma)|^2$ is the thrust of a single wing maintaining the follower's flapping amplitude $\tilde{A}_2$.

4.2.2. *Hydrodynamic potential, schooling numbers and 'keep-up' schooling condition*

We approximate the free-stream velocity on wing surfaces, $U_\infty + u$ in (4.2), by the wing swimming speed U_∞, ignoring the small perturbation in horizontal velocity u, as in the linearised calculation. The skin-friction $D_k(|U_\infty|)$, $k = 1, 2$ is then a function of U_∞ only. As the two wings swim at the same speed, they experience the same amount of drag $D_1 = D_2$. Note that the stroke-averaged thrust and drag are always balanced on the leader wing, $\langle T_1\rangle + D_1 = 0$ (4.19). It then follows that $0 = \langle T_1\rangle + D_1 = \langle T_1\rangle + D_2$. Using this relation and (4.58), we obtain the following expression for the total hydrodynamic force on the follower:

$$\langle F_2\rangle = \langle T_2\rangle + D_2 = \langle T_1\rangle\left[\varepsilon^2 + Q^2(\sigma) - 1 + 2\varepsilon\,Q(\sigma)\cos\left(2\pi\,\left(S - \delta_4(\sigma)\right)\right)\right]. \tag{4.63}$$

In figure 17(*a*), the approximation of the follower's drag $D_2 = -\langle T_1\rangle$, calculated by (4.9) (black dashed curve), is compared with the drag computed from the simulations (grey dashed curve), which shows the theoretical approximation is close to the simulation when the schooling number S is not too small, i.e. the follower is not too close to the

https://doi.org/10.1017/jfm.2026.11521 Published online by Cambridge University Press

leader. It then follows that the total hydrodynamic force formula (4.63) serves as a good approximation to the simulations, as shown in figure 17(*b*).

The hydrodynamic potential $\phi(S)$ is the negative integral of the the hydrodynamic force $\langle F_2\rangle$, given as

$$\phi(S) = -\int \langle F_2\rangle \,\mathrm{d}S = -\langle T_1\rangle \left[\left(\varepsilon^2 + Q^2(\sigma) - 1\right) S + \frac{\varepsilon Q(\sigma)}{\pi} \sin\left(2\pi\ (S - \delta_4(\sigma))\right)\right]. \tag{4.64}$$

In figures 17(*b*) and 17(*c*), the hydrodynamic force calculated from (4.63) and hydrodynamic potential from (4.64) are shown, and compared with simulations of two wings having the same flapping amplitude (the same simulation data as in figure 17*b*). Here, σ in (4.63)–(4.64) is solved from (4.19) given a flapping amplitude $\tilde{A} = 0.2$ and a drag coefficient $C_f = 0.02$. For other values of C_f (ranging from 0.01 to 0.1), the system also exhibits multiple stable equilibria, producing a corrugated potential landscape $\phi(S)$ characterised by an array of stable wells, similar to that shown in figure 17(*c*) (for $\varepsilon = 1$). The positions of the local minima shift only moderately with C_f, moving toward slightly smaller S as C_f increases. Moreover, the widths of these wells, which corresponds to their basins of attraction, show minimal variation with C_f.

The steady schooling numbers are roots of $\langle F_2\rangle$, or local extrema of $\phi(S)$, which can be solved from (4.63)

$$S_k^{\pm} = \pm\frac{1}{2\pi} \arccos\left(\frac{1 - \varepsilon^2 - Q^2(\sigma)}{2\varepsilon Q(\sigma)}\right) + q(\sigma) - \frac{\sigma}{\pi} + k, \quad k \in \mathbb{Z}^+. \tag{4.65}$$

Moreover, it can be shown from (4.64) that S_k^- are stable schooling numbers (stable critical points) and S_k^+ are unstable (see figure 18). If the two wings have the same flapping amplitude, $\varepsilon = \tilde{A}_2/\tilde{A}_1 = 1$, (4.65) simplifies to

$$S_k^{\pm} = \pm\frac{1}{2\pi} \arccos\left(-Q(\sigma)/2\right) + q(\sigma) - \frac{\sigma}{\pi} + k, \quad k \in \mathbb{Z}^+. \tag{4.66}$$

This is compared in figure 18(*a*,*b*) with simulations of two wings having the same flapping amplitude, where σ is solved from (4.19) given a flapping amplitude $\tilde{A}$ and a drag coefficient C_f. At the long wavelength limit $\sigma = \pi c/\lambda \to 0$, we have $Q(\sigma) \to 0$ and $q(\sigma) \to 1/2$, so that the schooling numbers achieve limits

$$S_k^- \to k + \frac{1}{4}, \quad S_k^+ \to k + \frac{3}{4}, \quad k \in \mathbb{Z}^+. \tag{4.67}$$

Note that if the two wings have different flapping amplitudes, (4.65) indicates a condition for steady schooling states, i.e.

$$-1 \leqslant \frac{1 - \varepsilon^2 - Q^2(\sigma)}{2\varepsilon Q(\sigma)} \leqslant 1. \tag{4.68}$$

This provides a 'keep-up' condition for the ratio of the follower's amplitude $\tilde{A}_2$ to the leader's amplitude $\tilde{A}_1$

$$1 - Q(\sigma) \leqslant \tilde{A}_2/\tilde{A}_1 \leqslant 1 + Q(\sigma). \tag{4.69}$$

As figure 18(*c*) shows, the schooling number exists only for $1 - Q(\sigma) \leqslant \varepsilon \leqslant 1 + Q(\sigma)$. Stable and unstable branches merge at $\varepsilon = 1 \pm Q(\sigma)$. It can also be seen in figure 17(*b*,*c*) that for $\varepsilon = 1 \pm Q(\sigma)$, the hydrodynamic force $\langle F_2\rangle$ in (4.63) has only one root in each

https://doi.org/10.1017/jfm.2026.11521 Published online by Cambridge University Press

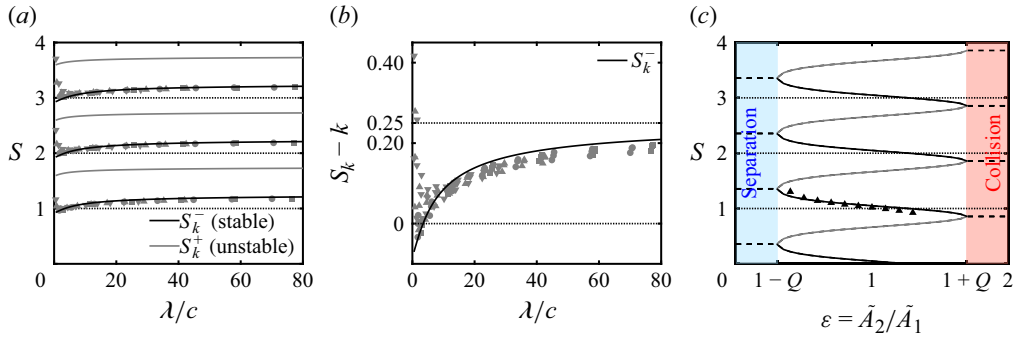


Figure 18. Schooling numbers computed from simulations (symbols) are compared with the linearised theory calculations (lines). Stable schooling numbers S_k^- are black and unstable schooling numbers S_k^+ are grey. (*a*)–(*b*) Flapping amplitudes are the same on both wings, the amplitude $\tilde{A}$ and drag coefficient C_f are varied. In (*b*), integers $k = 1, 2, 3$ are subtracted from stable schooling numbers S_k^-. The limit $S_k^- - k \to 1/4$ as $\lambda/c \to \infty$. The simulation data are the same as in figure 7. (*c*) Fix leader's amplitude $\tilde{A}_1 = 0.2$, and vary follower's amplitude $\tilde{A}_2$. Stable and unstable schooling numbers exist when $1 - Q \leqslant \tilde{A}_2/\tilde{A}_1 \leqslant 1 + Q$. The simulation data are the same as in figure 12(*a*). The drag coefficient is $C_f = 0.02$.

period, where the stable and unstable solutions collapse. Beyond the range of (4.69), $\langle F_2 \rangle$ does not intersect with the x-axis. When $\tilde{A}_2/\tilde{A}_1 < 1 - Q(\sigma)$, the hydrodynamic force on the follower wing is always strictly positive (always in the opposite direction of swimming). In this case, the follower cannot generate enough force maintaining the same swimming speed U_∞ as the leader, so that the follower is not able to 'keep up' in the school and will drift away downstream. It can also be explained by the hydrodynamic potential profile $\phi(S)$ in figure 17(*c*), that $\phi(S)$ is a monotonically decreasing function in S, and wherever the follower locates in this potential the schooling number S could not be trapped and will keep increasing. For $\tilde{A}_2/\tilde{A}_1 > 1 + Q(\sigma)$, the hydrodynamic force is always strictly negative (always in the swimming direction), therefore the follower will keep accelerating, eventually leading to 'rear-ending' collisions within the school. Tests with other values of skin-friction drag coefficient C_f show that the 'separation' and 'collision' regions (as in figure 18*c*) shrink as C_f increases. This indicates that the follower is more likely to maintain a stable formation with the leader at higher C_f, and that the schooling number exists over a wider range of ε, i.e. the stability of the schooling configuration improves with increasing C_f.

5. Discussion and conclusions

We have studied theoretically the hydrodynamics and locomotion dynamics of interacting flapping wings or foils in tandem. Numerical simulations show that the follower wing of a pair, when released to swim freely, tends to re-position itself within the leader's wake flow and lock into one of multiple positions. These emergent stable states correspond to so-called schooling numbers $S = g/\lambda$ near integer values, indicating that the follower takes up a separation distance g that is nearly an integer multiple of the swimming wavelength λ. This observation is consistent with previous experiments (Ramananarivo *et al.* 2016; Newbolt *et al.* 2019, 2024) and vortex-sheet simulations (Heydari & Kanso 2021; Nitsche *et al.* 2025). A systematic analysis of the stable configurations shows that the emergent S values are a weak function of λ, i.e. $S_k \approx S(\lambda) + k$, $k \in \mathbb{Z}^+$. We have also mapped out

https://doi.org/10.1017/jfm.2026.11521 Published online by Cambridge University Press

the hydrodynamic potential on the follower wing using two methods: one in which a fixed force is applied and the resulting position is determined, and the other in which a fixed position within the leader's wake is imposed and the resulting force is determined. Both methods show that the interaction potential resembles a tilted washboard: a series of local minima or stable wells, corresponding to the observed 'schooling' states, superposed on a potential that grows with the dimensionless separation distance S. The global minimum at $S \approx 0$ corresponds to a 'collision' of the two wings, and indeed simulations show that the follower rear ends the leader for some initialisations.

By computing and visualising the associated flow fields, we also determine some important mechanisms at work as the follower oscillates within the wave-like flow left by the leader. When the follower is at a position such that its vertical flapping velocity is instantaneously in phase with the vertical flow of the leader's wake, a low average thrust results. This synchronisation of follower-wake motions leads to a constructive interaction that generates a stronger collective wake, but also a weak thrust on the follower as its vertical velocity relative to the ambient fluid is decreased. In contrast, if the follower is at a position such that its vertical motion is out of phase with the leader's wake flow, we observe a destructive interaction, a weaker collective wake, higher follower-flow relative velocities and a maximum thrust. The equilibrium states are intermediate in these extremes and correspond to positions where the average thrust of the follower is largely unchanged relative to swimming in isolation. Importantly, the stability of observed schooling states is assured by a specific follower-wake phase relationship. At downstroke, for example, the follower sees a downward flow just upstream, so that if it were perturbed forward, its thrust would decrease, countering the perturbation. Similarly, upward flows just downstream of the follower ensure that perturbations that increase separation yield increased thrust and again a return to the stable equilibrium position.

These explorations also suggest that, through appropriate positioning within a leader's wake, a follower may take advantage of flow interactions. We demonstrate this for the case of a weakly flapping follower who may keep up with a faster flapping leader by exploiting its wake flow. This ability of a pair of uncoordinated flapping wings to move together cohesively due to the interaction of the follower with the wake left by the leader was also observed experimentally by Newbolt *et al.* (2019). We find that this 'freeloading' follower who flaps with smaller amplitude can travel up to four times faster than it would in isolation by taking up favourable positions in which it oscillates counter to the leader's wake flows. Further, the Froude efficiency of the follower is more than doubled and in some cases the follower's net energy is positive, which implies that energy could in principle be stored and used for other purposes. The leader is minimally affected, and so the efficiency of the pair is also improved.

For all these two-body interaction settings, the leader is affected much less, though some systematic trends are observed. We find that the leader's swimming speed, which is also that of the pair for the schooling states, decreases in comparison with isolated swimming. Interestingly, this decrease reflects an upstream influence due to the presence of the follower. When the follower is very close to the leader, the speed drops by as much as 50 %, and this decrease is only 10 % $\sim$ 20 % if the follower is one wavelength behind. The pair speed approaches the single-wing speed for large separations. This result is opposite to that observed in recent experiments (Ramananarivo *et al.* 2016) and simulations (Heydari & Kanso 2021), for which the leader's speed (and the pair speed) is somewhat faster than the single-wing speed, and smaller separations are associated with higher speeds. Later investigations found that the flow interactions have negligible effects on the speed of the pair (Newbolt *et al.* 2019; Nitsche *et al.* 2025).

https://doi.org/10.1017/jfm.2026.11521 Published online by Cambridge University Press

Using a linearised theory, we have also calculated the hydrodynamic forces and the hydrodynamic potential on the follower wing. The linearised theory assumes a small amplitude of wing flapping and a small Strouhal number of the swimming motion, and calculates the interaction of the follower wing with the wake shed by the leader. This linearised theory shows the hydrodynamic force on the follower is a sinusoidal function of period one in the schooling number, which agrees with our vortex-sheet simulations. Moreover, the maximum (minimum) of the hydrodynamic thrust produced by the follower is achieved when the wing–flow relative velocity achieves a maximum (minimum). An analytic form of the hydrodynamic potential is also calculated, from which the stable schooling numbers are solved and found to agree with the simulations for small Strouhal numbers. Both the simulations and the linearised theory agree well with the stable schooling numbers observed in experiments (Ramananarivo *et al.* 2016). For two wings having different flapping amplitudes, the linearised theory produces a condition for the follower to keep up with the leader, exploiting its wake for faster propulsion.

The case of two flapping wings is perhaps the simplest 'school' or 'flock' of interacting locomotors, and many elaborations might be considered for future study. One direction is to consider the influence of differing flapping kinematics on the emergent configurations and dynamics of a group, whether a pair or larger. This current work has shown the re-positioning that results from changing flapping amplitude alone. The experiments in Newbolt *et al.* (2019) showed that differing temporal phases lead to schooling states of different separations and different schooling numbers, and that stable positioning from differing flapping frequencies among individuals can still be achieved. Therefore, it would be interesting to derive a 'keep-up' condition for this scenario as well. The two-wing system can also inform the understanding of more complex, many-body configurations and the behaviour of more sophisticated locomotion systems. In a tandem or single-file arrangement, a third wing interacts with a flow that is the superposition of flows by both upstream neighbours, for example. The extent to which interactions are pairwise versus cumulative was investigated by Newbolt *et al.* (2024), who found that pairwise flow interactions promote orderly arrays or 'crystals' of individuals, but that this order can get disrupted by unstably growing positional waves. Results obtained either experimentally or numerically for few interacting bodies (Lin *et al.* 2020, 2024; Heydari, Hang & Kanso 2024; Newbolt *et al.* 2024; Nitsche *et al.* 2025) could still benefit from a rigorous analysis of the pairwise interactions.

Recent works have also explored pairs of self-propelled, inline plates with pitching motions. A numerical study by Heydari & Kanso (2021) revealed that these motions significantly enhance the group's swimming efficiency compared with when the plates swim in isolation. Such improvements in efficiency can also occur with mismatched foil pitching amplitudes (Han *et al.* 2025). A range of flow conditions, including phase synchrony and pitching amplitude, was shown to lead to 2-D stability of various formations in recent experiments on the self-organisation of a pair of pitching hydrofoils (Ormonde *et al.* 2024). Therefore, it would be interesting to explore 2-D configurations in which heaving-and-pitching individuals are spaced laterally and perhaps allowed to move laterally or reorient due to the flow interactions. These elaborations could shed light on classical models of 2-D fish schools and indeed on the flows and dynamics of collectively swimming and flying animals.

Supplementary movie. Supplementary movie is available at https://doi.org/10.1017/jfm.2026.11521.

Acknowledgements. We thank S. Ramananarivo, A. Oza, J. W. Newbolt, S. Childress and J. Zhang for fruitful discussions of the modelling, and thank M. O'Neil, S. Tang and A. Rahimian for discussions of numerical quadratures. This work was supported by the Lyttle Chair in Applied Mathematics to M.S. and the

https://doi.org/10.1017/jfm.2026.11521 Published online by Cambridge University Press

U.S. National Science Foundation award DMS-1847955 to L.R. For the purpose of Open Access, the authors will apply a CC BY public copyright licence to any Author Accepted Manuscript version arising from this submission.

Declaration of interests. The authors report no conflicts of interest.

Appendix A. Vortex-sheet model

In the vortex-sheet simulation, high-order quadrature rules for the Cauchy singular integrals (2.15) must be applied to prevent the free vortex sheet of the leader wing penetrating the bound vortex sheet of the follower wing. In this section, we propose two quadrature rules for the influence of the bound sheet and free sheet, respectively. First, a singularity subtraction technique is proposed for the bound vortex sheet, which is accurate for polynomial approximations of the vortex-sheet strength $\bar{\gamma}(s)$. This quadrature allows us to calculate the velocity induced by the bound vortex sheet (approximated by polynomials) accurately at any point off the boundary. Second, for the free vortex sheet, we analytically calculate the velocity induced by each vortex-sheet segment, the sum of which provides the velocity field induced by the full free vortex sheet.

A.1. *Singularity subtraction method for the bound vortex-sheet integral*

We first consider a general Cauchy integral of the form

$$G(z) = \int_{-1}^{1} \frac{\gamma(s)}{z-s}\,\mathrm{d}s, \quad \text{for } z \notin [-1,\,1], \tag{A1}$$

where $z = x + iy$ is a complex point not on the finite segment $[-1,\,1]$, and $\gamma(s)$ is a real function. Equation (A1) is also called the finite Hilbert transform of the real function $\gamma(s)$ (King 2009; Olver 2011). In our vortex-sheet model, if we assume that the position of the rigid bound vortex sheet is

$$\xi(s) = c + \hat{s}s, \ \text{where } c = \xi(0), \ \text{ and } \ -1 \leqslant s \leqslant 1, \tag{A2}$$

then the velocity field induced by the bound vortex sheet (2.15) is expressed as

$$I_b(z) = \frac{1}{2\pi i}\int_{-1}^{1} \frac{\gamma(s)}{z-\xi(s)}\,\mathrm{d}s = \frac{1}{2\pi i}\frac{1}{\hat{s}}\int_{-1}^{1} \frac{\gamma(s)}{(z-c)/\hat{s}-s}\,\mathrm{d}s = \frac{1}{2\pi i}\frac{1}{\hat{s}}G\left(\frac{z-c}{\hat{s}}\right). \tag{A3}$$

Here, $\hat{s}$ denotes the tangential direction of the wing. In the following subsection, we show the singularity subtraction method for calculating the Hilbert transform (A1).

A.1.1. *The case where $\gamma(s)$ is a polynomial*

Assume $\gamma(s)$ is a polynomial, which could be a polynomial interpolation of some function. In (A1), we separate the singular part manually by subtracting the constant $\gamma(z)$ from $\gamma(s)$. The integral then splits into two parts

$$\begin{aligned} G(z) = \int_{-1}^{1} \frac{\gamma(s)}{z-s}\,\mathrm{d}s &= -\int_{-1}^{1} \frac{\gamma(s)-\gamma(z)}{s-z}\,\mathrm{d}s + \gamma(z)\int_{-1}^{1} \frac{1}{z-s}\,\mathrm{d}s \\ &= -\int_{-1}^{1} g(s)\,\mathrm{d}s - \gamma(z)\log\frac{1-z}{1+z}. \end{aligned} \tag{A4}$$

The first part is a regular integral of the smooth function $g(s)$, given by

$$g(s) = \frac{\gamma(s)-\gamma(z)}{s-z}. \tag{A5}$$

https://doi.org/10.1017/jfm.2026.11521 Published online by Cambridge University Press

In fact, if we assume $\gamma(s)$ is a polynomial of a real variable s with real coefficients, then $g(s)$ is a polynomial of real s, while the coefficients are polynomials of complex variable z. Therefore, high-order quadrature rules such as Gauss–Legendre quadrature or Clenshaw–Curtis quadrature can be applied, both of which provide accurate evaluations for polynomials (Trefethen 2008).

A.1.2. *The case where $\nu(s)=\gamma(s)\sqrt{1-s^2}$ is a polynomial*

In the vortex-sheet simulations, the true vortex-sheet strength contains an inverse-square-root singularity at the wing leading edge, which can be expressed as

$$\gamma(s)=\frac{\nu(s)}{\sqrt{1-s^2}},\quad -1\leqslant s\leqslant 1, \tag{A6}$$

where $\nu(s)$ can be a smooth function. Now we consider the following singular integral:

$$G(z)=\int_{-1}^{1}\frac{\nu(s)}{\sqrt{1-s^2}\,(z-s)}\,\mathrm{d}s,\quad \text{for } z\notin[-1,\,1], \tag{A7}$$

and assume $\nu(s)$ is a polynomial. In our vortex-sheet method, it is a polynomial interpolation on Chebyshev–Gauss–Lobatto nodes (2.29).

Using the singularity subtraction trick, we have

$$\begin{aligned}G(z)=\int_{-1}^{1}\frac{\nu(s)}{\sqrt{1-s^2}\,(z-s)}\,\mathrm{d}s&=-\int_{-1}^{1}\frac{1}{\sqrt{1-s^2}}\frac{\nu(s)-\nu(z)}{s-z}\,\mathrm{d}s+\int_{-1}^{1}\frac{\nu(z)}{\sqrt{1-s^2}\,(z-s)}\,\mathrm{d}s\\&=-\int_{-1}^{1}\frac{g(s)}{\sqrt{1-s^2}}\,\mathrm{d}s+\nu(z)\int_{-1}^{1}\frac{1}{\sqrt{1-s^2}\,(z-s)}\,\mathrm{d}s,\end{aligned} \tag{A8}$$

where $g(s)=(\nu(s)-\nu(z))/(s-z)$ is a polynomial of s with complex coefficients that are polynomials of z. We evaluate the integral of $g(s)$ using Chebyshev quadrature at Chebyshev–Gauss–Lobatto nodes (2.29), which is accurate for polynomials (Mason & Handscomb 2002). The second term can be calculated analytically (Golberg 2013, p. 201)

$$\int_{-1}^{1}\frac{1}{\sqrt{1-s^2}\,(z-s)}\,\mathrm{d}s=\frac{\pi}{\sqrt{z+1}\sqrt{z-1}},\quad \text{for } z\notin[-1,\,1]. \tag{A9}$$

A.2. *Quadrature for the free vortex sheet*

Now we discuss the quadrature on the free vortex sheet C_{fr}: $s_{min}\leqslant s\leqslant s_{max}$, for evaluating the potential flow induced by this sheet. Denote the position of the sheet by $\xi(s)$ and the arc length by s. Consider the following integral on C_{fr} for the smooth real function $\gamma(s)$:

$$I(z)=\int_{s_{min}}^{s_{max}}\frac{\gamma(s)}{z-\xi(s)}\,\mathrm{d}s,\quad z\notin[-1,\,1]. \tag{A10}$$

We discretise the boundary C_{fr} at $\xi_k=\xi(s_k),\ k=1,\ldots,N$, and let

$$\gamma_k=\int_{s_k}^{s_{k+1}}\gamma(s)\,\mathrm{d}s/(s_{k+1}-s_k) \tag{A11}$$

denote the average of γ on each piece. The boundary C_{fr} can be approximated by a piece-wise linear segment

$$\tilde{\xi}(s)\simeq p_k s+q_k,\quad \text{for } s_k\leqslant s\leqslant s_{k+1}, \tag{A12}$$

https://doi.org/10.1017/jfm.2026.11521 Published online by Cambridge University Press

where $\tilde{\xi}(s_k) = \xi_k$ are the endpoints of each segment. On each segment, $\gamma(s)$ is approximated by a piece-wise constant function

$$\tilde{\gamma}(s) \simeq \gamma_k, \quad \text{for } s_k \leqslant s \leqslant s_{k+1}. \tag{A13}$$

Next, we approximate the integral (A10) by the integral of $\tilde{\gamma}$ on $\tilde{\xi}$, which can be evaluated analytically. The integral (A10) can be written as the sum of integral contributions on each discrete piece, and then be approximated as

$$I(z) = \int_{s_{min}}^{s_{max}} \frac{\gamma(s)}{z - \xi(s)}\,\mathrm{d}s = \sum_{k=1}^{N-1} \int_{s_k}^{s_{k+1}} \frac{\gamma(s)}{z - \xi(s)}\,\mathrm{d}s = \sum_{k=1}^{N-1} I_k(z), \tag{A14}$$

where

$$I_k(z) = \int_{s_k}^{s_{k+1}} \frac{\gamma(s)}{z - \xi(s)}\,\mathrm{d}s \simeq \int_{s_k}^{s_{k+1}} \frac{\gamma_k}{z - q_k - p_k s}\,\mathrm{d}s = \frac{\gamma_k}{p_k} \log\left(\frac{z - \xi_k}{z - \xi_{k+1}}\right), \tag{A15}$$

and $p_k = (\xi_{k+1} - \xi_k)/(s_{k+1} - s_k)$. Therefore, the integral on the boundary (A10) is approximated as

$$I(z) \simeq \sum_{k=1}^{N-1} \frac{(s_{k+1} - s_k)\gamma_k}{\xi_{k+1} - \xi_k} \log\left(\frac{z - \xi_k}{z - \xi_{k+1}}\right). \tag{A16}$$

We note that $(s_{k+1} - s_k)\gamma_k$ denotes the circulation on the vortex-sheet segment $[\xi_k, \xi_{k+1}]$, which is the unnormalised vortex-sheet strength; see § 2. It can be shown that the piece-wise quadrature on the free vortex sheet is first-order accurate.

References

Abramowitz, M. & Stegun, I.A. 1964 *Handbook of Mathematical Functions with Formulas, Graphs, and Mathematical Tables. National Bureau of Standards Applied Mathematics Series* 55. U.S. Government Printing Office.

Akhtar, I., Mittal, R., Lauder, G.V. & Drucker, E. 2007 Hydrodynamics of a biologically inspired tandem flapping foil configuration. *Theor. Comput. Fluid Dyn.* **21** (3), 155–170.

Alben, S. 2009*a* On the swimming of a flexible body in a vortex street. *J. Fluid Mech.* **635**, 27–45.

Alben, S. 2009*b* Simulating the dynamics of flexible bodies and vortex sheets. *J. Comput. Phys.* **228** (7), 2587–2603.

Alben, S. 2009*c* Wake-mediated synchronization and drafting in coupled flags. *J. Fluid Mech.* **641**, 489–496.

Alben, S. 2010*a* Passive and active bodies in vortex-street wakes. *J. Fluid Mech.* **642**, 95–125.

Alben, S. 2010*b* Regularizing a vortex sheet near a separation point. *J. Comput. Phys.* **229** (13), 5280–5298.

Alben, S. 2012 Flapping propulsion using a fin ray. *J. Fluid Mech.* **705**, 149–164.

Alben, S. & Shelley, M. 2005 Coherent locomotion as an attracting state for a free flapping body. *Proc. Natl Acad. Sci. USA* **102** (32), 11163–11166.

Alben, S. & Shelley, M.J. 2008 Flapping states of a flag in an inviscid fluid: bistability and the transition to chaos. *Phys. Rev. Lett.* **100** (7), 074301.

Becker, A.D., Masoud, H., Newbolt, J.W., Shelley, M. & Ristroph, L. 2015 Hydrodynamic schooling of flapping swimmers. *Nat. Commun.* **6**, 1–8.

Belyayev, V.V. & Zuyev, G.V. 1969 Hydrodynamic hypothesis of school formation in fishes. *J. Ichthyol.* **9**, 578–584.

Boschitsch, B.M., Dewey, P.A. & Smits, A.J. 2014 Propulsive performance of unsteady tandem hydrofoils in an in-line configuration. *Phys. Fluids* **26** (5), 051901.

Broyden, C.G. 1965 A class of methods for solving nonlinear simultaneous equations. *Math. Comput.* **19** (92), 577–593.

Carrier, J., Greengard, L. & Rokhlin, V. 1988 A fast adaptive multipole algorithm for particle simulations. *SIAM J. Sci. Stat. Comput.* **9** (4), 669–686.

Daghooghi, M. & Borazjani, I. 2015 The hydrodynamic advantages of synchronized swimming in a rectangular pattern. *Bioinspir. Biomim.* **10** (5), 056018.

https://doi.org/10.1017/jfm.2026.11521 Published online by Cambridge University Press

DEWEY, P.A., QUINN, D.B., BOSCHITSCH, B.M. & SMITS, A.J. 2014 Propulsive performance of unsteady tandem hydrofoils in a side-by-side configuration. *Phys. Fluids* **26** (4), 041903.
DIMITRIADIS, G., GARDINER, J.D., TICKLE, P.G., CODD, J. & NUDDS, R.L. 2015 Experimental and numerical study of the flight of geese. *Aeron. J.* **119** (1217), 803–832.
FANG, F., HO, K.L., RISTROPH, L. & SHELLEY, M. 2017 A computational model of the flight-dynamics and aerodynamics of a jellyfish-like flying machine. *J. Fluid Mech.* **819**, 621–655.
GAZZOLA, M., ARGENTINA, M. & MAHADEVAN, L. 2014 Scaling macroscopic aquatic locomotion. *Nat. Phys.* **10** (10), 758–761.
GOLBERG, M.A. 2013 *Numerical Solution of Integral Equations*, vol. 42. Springer Science & Business Media.
GREENEWALT, C.H. 1962 Dimensional relationships for flying animals. *Smithsonian miscellaneous collections*.
HAN, T., MIVEHCHI, A., SARRAF, S.S. & MOORED, K.W. 2025 Tailoring formations of self-organising hydrofoil schools towards high-efficiency. *J. Fluid Mech.* **1012**, A26.
HEMELRIJK, C.K., REID, D.A.P., HILDENBRANDT, H. & PADDING, J.T. 2015 The increased efficiency of fish swimming in a school. *Fish Fisheries* **16** (3), 511–521.
HEYDARI, S., HANG, H. & KANSO, E. 2024 Mapping spatial patterns to energetic benefits in groups of flow-coupled swimmers. *eLife* **13**, RP96129.
HEYDARI, S. & KANSO, E.2021 School cohesion, speed and efficiency are modulated by the swimmers flapping motion. *J. Fluid Mech.* **922**, A27.
JONES, M.A. 2003 The separated flow of an inviscid fluid around a moving flat plate. *J. Fluid Mech.* **496**, 405–441.
JONES, M.A. & SHELLEY, M.J. 2005 Falling cards. *J. Fluid Mech.* **540**, 393–425.
KILLEN, S.S., MARRAS, S., STEFFENSEN, J.F. & MCKENZIE, D.J. 2012 Aerobic capacity influences the spatial position of individuals within fish schools. *Proc. Biol. Sci.* **279** (1727), 357–364.
KING, F.W. 2009 *Hilbert Transforms. Encyclopedia of Mathematics and its Applications 1*. Cambridge University Press.
KRASNY, R. 1986 Desingularization of periodic vortex sheet roll-up. *J. Comput. Phys.* **65** (2), 292–313.
KRISHNAN, K., *et al.* 2022 The role of wingbeat frequency and amplitude in flight power. *J. R. Soc. Interface* **19** (193), 20220168.
LIAO, J.C. 2007 A review of fish swimming mechanics and behaviour in altered flows. *Phil. Trans. R. Soc. Lond. B: Biol. Sci.* **362** (1487), 1973–1993.
LIAO, J.C., BEAL, D.N., LAUDER, G.V. & TRIANTAFYLLOU, M.S. 2003 Fish exploiting vortices decrease muscle activity. *Science* **302** (5650), 1566–1569.
LIGHTHILL, M.J. 1960 Note on the swimming of slender fish. *J. Fluid Mech.* **9** (02), 305–317.
LIN, X., LIU, Y. & WU, J. 2024 Various and orderly formations in the hydrodynamic schooling of multiple flapping swimmers. *Phys. Fluids* **36** (8), 081902.
LIN, X., WU, J., ZHANG, T. & YANG, L. 2020 Self-organization of multiple self-propelling flapping foils: energy saving and increased speed. *J. Fluid Mech.* **884**, R1.
LISSAMAN, P.B.S. & SHOLLENBERGER, C.A. 1970 Formation flight of birds. *Science* **168** (3934), 1003–1005.
MASON, J.C. & HANDSCOMB, D.C. 2002 *Chebyshev Polynomials*. CRC Press.
MAVROYIAKOUMOU, C., WU, J. & RISTROPH, L. 2025 Modeling flying formations as flow-mediated matter. arXiv:2506.14025.
MOORE, D.W. 1979 The spontaneous appearance of a singularity in the shape of an evolving vortex sheet. *Proc. R. Soc. Lond. A* **365**, 105–119.
MÜLLER, U.K., VAN DEN HEUVEL, B.L.E., STAMHUIS, E.J. & VIDELER, J.J. 1997 Fish foot prints: morphology and energetics of the wake behind a continuously swimming mullet (*Chelon labrosus* risso). *J. Exp. Biol.* **201**, 2893–2906.
NEWBOLT, J.W., LEWIS, N., BLEU, M., WU, J., MAVROYIAKOUMOU, C., RAMANANARIVO, S. & RISTROPH, L. 2024 Flow interactions lead to self-organized flight formations disrupted by self-amplifying waves. *Nat. Commun.* **15** (1), 3462.
NEWBOLT, J.W., ZHANG, J. & RISTROPH, L. 2019 Flow interactions between uncoordinated flapping swimmers give rise to group cohesion. *Proc. Nat. Acad. Sci.* **116** (7), 2419–2424.
NITSCHE, M. & KRASNY, R. 1994 A numerical study of vortex ring formation at the edge of a circular tube. *J. Fluid Mech.* **276**, 139–161.
NITSCHE, M., OZA, A.U. & SIEGEL, M. 2025 On the stability of an in-line formation of hydrodynamically interacting flapping plates. *J. Fluid Mech.* **1013**, A14.
OLVER, S. 2011 Computing the Hilbert transform and its inverse. *Math. Comput.* **80** (275), 1745–1767.

https://doi.org/10.1017/jfm.2026.11521 Published online by Cambridge University Press

ORMONDE, P.C., KURT, M., MIVEHCHI, A. & MOORED, K.W. 2024 Two-dimensionally stable self-organisation arises in simple schooling swimmers through hydrodynamic interactions. *J. Fluid Mech.* **1000**, A90.

OZA, A.U., RISTROPH, L. & SHELLEY, M.J. 2019 Lattices of hydrodynamically interacting flapping swimmers. *Phys. Rev. X* **9** (4), 041024.

PARTRIDGE, B.L. & PITCHER, T.J. 1979 Evidence against a hydrodynamic function for fish schools. *Nature* **279** (5712), 418–419.

PORTUGAL, S.J., HUBEL, T.Y., FRITZ, J., HEESE, S., TROBE, D., VOELKL, B., HAILES, S., WILSON, A.M. & USHERWOOD, J.R. 2014 Upwash exploitation and downwash avoidance by flap phasing in ibis formation flight. *Nature* **505** (7483), 399–402.

RAMANANARIVO, S., FANG, F., OZA, A., ZHANG, J. & RISTROPH, L. 2016 Flow interactions lead to orderly formations of flapping wings in forward flight. *Phys. Rev. Fluids* **1** (7), 071201.

RAYNER, J.M.V. 1979 A new approach to animal flight mechanics. *J. Exp. Biol.* **80** (1), 17–54.

RISTROPH, L. & ZHANG, J. 2008 Anomalous hydrodynamic drafting of interacting flapping flags. *Phys. Rev. Lett.* **101** (19), 194502.

ROSENHEAD, L. 1931 The formation of vortices from a surface of discontinuity. *Proc. R. Soc. Lond. A* **134** (823), 170–192.

SAFFMAN, P.G. 1993 *Vortex Dynamics*. Cambridge University Press.

SCHLICHTING, H. 1968 *Boundary-Layer Theory*. McGraw-Hill.

SHELLEY, M.J. 1992 A study of singularity formation in vortex-sheet motion by a spectrally accurate vortex method. *J. Fluid Mech.* **244**, 493–526.

SHYY, W., AONO, H., CHIMAKURTHI, S.K., TRIZILA, P., KANG, C.-K., CESNIK, C.E.S. & LIU, H. 2010 Recent progress in flapping wing aerodynamics and aeroelasticity. *Prog. Aerosp. Sci.* **46** (7), 284–327.

SVENDSEN, J.C., SKOV, J., BILDSOE, M. & STEFFENSEN, J.F. 2003 Intra-school positional preference and reduced tail beat frequency in trailing positions in schooling roach under experimental conditions. *J. Fish Biol.* **62** (4), 834–846.

TAYLOR, L.A., TAYLOR, G.K., LAMBERT, B., WALKER, J.A., BIRO, D. & PORTUGAL, S.J. 2019 Birds invest wingbeats to keep a steady head and reap the ultimate benefits of flying together. *PLOS Biol.* **17** (6), e3000299.

TREFETHEN, L.N. 2008 Is Gauss quadrature better than Clenshaw-Curtis? *SIAM Rev.* **50** (1), 67–87.

VANDENBERGHE, N., CHILDRESS, S. & ZHANG, J. 2006 On unidirectional flight of a free flapping wing. *Phys. Fluids* **18** (1), 014102.

VANDENBERGHE, N., ZHANG, J. & CHILDRESS, S. 2004 Symmetry breaking leads to forward flapping flight. *J. Fluid Mech.* **506**, 147–155.

VISCOR, G. & FUSTER, J.F. 1987 Relationships between morphological parameters in birds with different flying habits. *Compar. Biochem. Physiol. A: Physiol.* **87** (2), 231–249.

WEIHS, D. 1973 Hydrodynamics of fish schooling. *Nature* **241**, 290–291.

WEIHS, D. 1975 Some hydrodynamical aspects of fish schooling. In *Swimming and Flying in Nature*, pp. 703–718. Springer.

WEIMERSKIRCH, H., MARTIN, J., CLERQUIN, Y., ALEXANDRE, P. & JIRASKOVA, S. 2001 Energy saving in flight formation. *Nature* **413** (6857), 697–698.

WU, T.Y. 1961 Swimming of a waving plate. *J. Fluid Mech.* **10** (03), 321–344.

WU, T.Y. 1972 Extraction of flow energy by a wing oscillating in waves. *J. Ship Res.* **16** (01), 66–78.

WU, T.Y. & CHWANG, A.T. 1975 Extraction of flow energy by fish and birds in a wavy stream. In *Swimming and Flying in Nature*, pp. 687–702. Springer.

ZHU, X., HE, G. & ZHANG, X. 2014 Flow-mediated interactions between two self-propelled flapping filaments in tandem configuration. *Phys. Rev. Lett.* **113** (23), 238105.

ZUYEV, G.V. & BELYAYEV, V.V. 1970 An experimental study of the swimming of fish in groups as exemplified by the horsemackerel. *J. Ichthyol.* **10**, 545–549.

https://doi.org/10.1017/jfm.2026.11521 Published online by Cambridge University Press